Cation-Induced Fibrillation of Microbial Glycolipid Biosurfactant Probed by Ion-Resolved In Situ SAXS

Alexandre Poirier, Patrick Le Griel, Javier Perez, Niki Baccile

Cation-Induced Fibrillation of Microbial Glycolipid Biosurfactant Probed by Ion-Resolved *In Situ* SAXS

Alexandre Poirier,[a] Patrick Le Griel,[a] Javier Perez, [b] Niki Baccile,[a,*]

Sorbonne Université, Laboratoire de Chimie de la Matière Condensée de Paris (LCMCP), UMR CNRS 7574, 4 place Jussieu, Paris, F-75005, France

E-mail: niki.baccile@sorbonne-universite.fr

[b] SWING Beamline, Soleil synchrotron, L'Orme des Merisiers, 91190 Saint-Aubin, France

Abstract

Biological amphiphiles are molecules with a rich phase behaviour. Micellar, vesicular and even fibrillar phases can be found for the same molecule by applying a change in pH or selecting the appropriate metal ion. The rich phase behaviour paves the way towards a broad class of soft material, from carriers to hydrogels. The present work contributes to understand the fibrillation of a microbial glycolipid, glucolipid G-C18:1 produced by *Starmerella bombicola ΔugtB1*, characterized by a micellar phase at alkaline pH and a vesicular phase at acidic pH. Fibrillation and prompt hydrogelation is triggered by adding either alkaline earth, Ca^{2+}, or transition metal, Ag^{+}, Fe^{2+}, Al^{3+}, ions to a G-C18:1 micellar solution. A specifically-designed apparatus coupled to a synchrotron SAXS beamline allows performing a simultaneous cation- and pH-resolved *in situ* monitoring of the morphological evolution from spheroidal micelles to crystalline fibers, when Ca^{2+} is employed, or to wormlike aggregates, when Fe^{2+} or Al^{3+} solutions are employed. The fast reactivity of Ag^{+} and the crystallinity of Ca^{2+}-induced fibers suggest that fibrillation is driven by direct metal-ligand interactions, while the shape transition from spheroidal to elongated micelles with Fe^{2+} or Al^{3+} rather suggest charge screening between the lipid and the hydroxylated cation species.

Introduction

Biobased surfactants are a family of amphiphilic molecules, which can be produced by chemical, enzymatic or microbial processes using processed biomass.[1] Besides their entirely bio-based production, surfactants produced by fermentation are certainly the most promising class of compounds able to replace synthetic surfactants.[2–4] Historically developed to replace

petrochemical surfactants, biological amphiphiles, also known as biosurfactants, are produced by the fermentation process of yeasts or bacteria in the presence of sugar and fatty acids.[3,4] So far, a number of properties (detergents, emulsion stabilizers, depollution, antimicrobials) and potential domains of applications (food science, environmental remediation, cosmetics, agricultural science)[5–7] have been developed. Since two decades, biosurfactants are a trendy topic, in particular for their high biocompatible and biodegradable character but also for their unique self-assembly properties.[8] Among the more classical micellar, vesicular or lamellar phases, expected for surfactants and lipids, some of them have shown the possibility to self-assemble into fibers, so to form a self-assembled fibrillar network (SAFiN), generally leading to hydrogels.[9–12] In this regard, biosurfactants could also be described as low-molecular weight gelators (LMWG).[13,14] Differently than polymer gels, LMWG exhibit a reversible and fast sol-gel transition, often driven by external stimuli such as temperature, pH or light.[15–17]

Fibrillation and sol-gel transitions in LMW amphiphiles[18–20] or amphiphilic polymers[21] can also be triggered by alkaline earth[22–24] or transition metal salts.[25–27] Supramolecular metallogels receive nowadays a growing interest for their potential applications in many areas, like medicine, drug delivery, environmental remediation, catalysis, electronics.[28–30] The growing interest of this family of gels comes from both the stimuli-responsiveness of the supramolecular self-assembly, and the interesting properties of the metal complex.[13,31] The typical phase transitions induced by salt in amphiphilic systems strongly depend on the type of ion.[32] For surfactants, typical evolutions are observed from spheres to cylinders[33–35] and wormlike morphologies,[36,37] from micelles to vesicles[38,39] or lamellae.[40] For other LMW compounds, like peptide amphiphiles, peptide derivatives or bile salts, fibrillation often occurs.[24,41–45] By salt addition, one can differentiate several mechanisms, possibly occurring simultaneously, at the origin of the morphological changes: charge screening,[46] bridging[47] or complexation.[48,49]

Recent work has shown that microbial glycolipid amphiphiles self-assemble into micelles at basic pH,[50,51] vesicles and lamellar phase at acidic pH.[50–52] In particular, the monounsaturated glycolipid, glucolipid G-C18:1 (Figure 1a), obtained by the fermentation of *Starmerella bombicola ΔugtB1* fed with glucose and vegetable oil,[51,53] was shown to form SAFiN[54] metallogels upon addition of a wide range of cations to its micellar phase, except Na^+, which has no impact on the phase behaviour (Figure 1b).[55,56] This result is unusual because fibrillation of surfactants driven by multivalent cations is not expected (literature survey can be found elsewhere).[55] Among all cations tested, two main structures could be observed by applying the combination of cryogenic transition electron microscopy (cryo-TEM) and small

angle X-ray scattering (SAXS) on metallogel samples. Ca^{2+} and Ag^{+}, but also Cr^{2+} or Mn^{2+}, induce fibrillation of G-C18:1 (Figure 1b), where fibers have both internal and suprafibrillar crystallinity, the former showing a rare side-by-side association of the fibers into β-sheet like rafts.[54,55] Fe^{2+} and Al^{3+}, as well as Cu^{2+}, Co^{2+} or Ni^{2+}, induce an elongation of the micelles (Figure 1b) and eventual percolated micellar network.[55]

Several studies have explored the interaction between microbial biosurfactants and ions.[57–61] If some of these studies tackle depollution from heavy metals,[58,59,62] others address the effect of the cations on the self-assembly properties.[57,63–65] However, the number of studies is small compared to the effect of cations on surfactant and lipids, and only limited effects on the micellar morphology have been reported so far. For instance, calcium ions have only shown to screen repulsive negative charges between sophorolipid or rhamnolipid micelles, with no effect on the phase behaviour.[57,63] In this context, the effect of cations on the self-assembly, structure and macroscale hydrogelation of G-C18:1 is quite unique, both compared to other biosurfactants, but also to amphiphiles in general.[66]

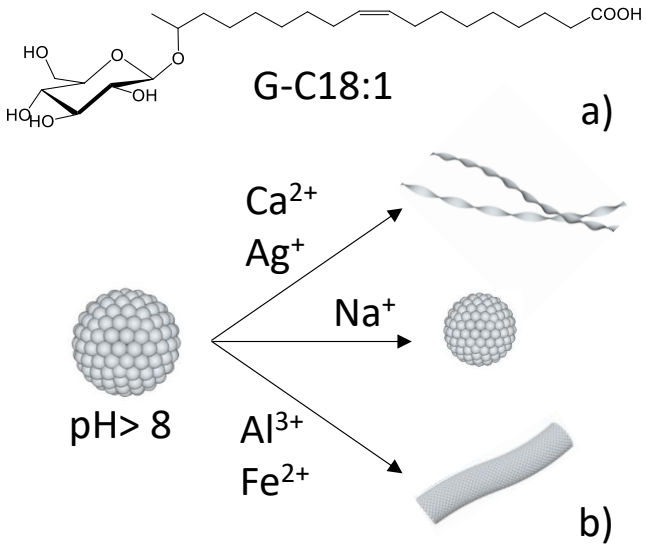

Figure 1 – a) Structure of G-C18:1 glycolipid bolaform amphiphile. b) Known phase behavior of G-C18:1 in water (pH> 8) at room temperature and G-C18:1 concentration below 5 wt%.[54,55]

For these reasons, this work is dedicated to explore the cation-induced fibrillation and micellization from a dynamic point of view, by mean of cation- and pH-resolved *in situ* SAXS experiments, performed on diluted metal-G-C18:1 solutions. On the basis of previous work,[55] Ag^{+} and Ca^{2+} are chosen to represent typical fibrillar structures, while Fe^{2+} and Al^{3+} to represent the typical micellar structures (Figure 1b). *In situ* SAXS using synchrotron radiation is a niche, although very powerful, characterization technique, employed since decades to explore fast

kinetics processes in soft and condensed matter.[67,68] Self-assembly using *in situ* SAXS is studied in materials as diverse as nanocelluloses,[69] lipids,[67] surfactants,[70] liquid crystalline colloids,[71] complex silica-surfactant hybrids,[72] but also cation-induced vesicle-to-hexagonal phase transition.[73]

Most of the cited works employ a stop-flow device,[70] which allows a time-resolved study of two solutions after fast mixing. Instead, the sample environment setup employed in this work has been adapted from previous pH-resolved *in situ* SAXS experiments performed on similar systems,[10,51,72,74] and consisting in a continuous addition of a salt into a lipid solution at a constant rate. Volumes are in milliliter range, rather than in the microliter for stop-flow, and the mixed solution is continuously stirred and flushed in front of the X-ray beam. If this method does not provide access to the initial stages of the self-assembly process, it represents very well a typical real-life laboratory process and it allows to monitor pH in real time. More specifically, the effect of controlled injections of salts of Ag^{+}, Ca^{2+}, Fe^{2+} or Al^{3+} on the self-assembled morphology of G-C18:1 and pH are monitored *in situ* in a continuous fashion. The data are correlated with complementary cryo-TEM, oscillatory rheology and calorimetry experiments performed elsewhere.[55,56]

Materials and methods

Chemicals. The monounsaturated glucolipid G-C18:1 (M_w = 460 g.mol^{-1}) contains a β-D-glucose unit covalently linked to oleic acid. The molecule is obtained by fermentation from of the yeast *Starmerella bombicola (ΔugtB1)* according the protocol given before.[51,53] The compound is purchased from the Bio Base Europe Pilot Plant, Gent, Belgium, lot N° APS F06/F07, Inv96/98/99 and used as such. According to the specification sheet provided by the producer, the batch (99.4% dry matter) is composed of 99.5% of G-C18:1, according to HPLC-ELSD chromatography data. NMR analysis was performed elsewhere.[50] NaOH (≥98wt% pellets), $FeCl_2.4H_2O$ (≥ 99wt%) and $AgNO_3$ are purchased from Sigma Aldrich; calcium chloride in pellets and HCl (35 wt%) are purchased from VWR. $AlCl_3.6H_2O$ (≥99wt%) is purchased from Acros Organics.

Sample preparation. G-C18:1 is dispersed in milli-Q water and the pH is adjusted by an initial addition of concentrated NaOH (5 M), followed by a refinement with few µL of more diluted NaOH (or HCl) solution (1 M, 0.5 M or 0.1 M). The targeted molecular ratio to be roughly in the region of pH 8 is [NaOH]:[G-C18:1]= 0.7–0.8. Salts solution are prepared at 1 M and added to the G-C18:1 solution so to reach the chosen cation-to-G-C18:1 ratio, provided in the main text. Typically, for a total 1 mL volume, 62.5 µL of AgNO3 (1 M), or 40 µL of CaCl2 (1 M), are added to the complementary volume of 3 wt% G-C18:1 in order to reach [$AgNO_3$]/[G-C18:1] = 1.0 and [$CaCl_2$]/[G-C18:1] = 0.6, respectively. A similar procedure is employed for all cations with [$AlCl_3$]/[G-C18:1] = 0.34 and [$FeCl_2$]/[G-C18:1] = 1.4. The solution is homogenized by vortexing (about 30 s). For light scattering and *in situ* SAXS experiment, the G-C18:1 concentration is $C_{G\text{-}C18:1}$= 0.5 wt%, while the concentrations of the cation solutions are 0.5 M for Ca^{2+}, Al^{3+} and Fe^{2+}, respectively. For rheology experiments, $C_{G\text{-}C18:1}$= 3 wt%. In this work, samples are labelled as follows, {M^{z+}}G-C18:1, with M^{z+}= Ca^{2+}, Ag^{+}, Al^{3+} and Fe^{2+}.

Throughout the text, the salt-to-lipid ratios are provided either in the form cation-to-G-C18:1 ratio, [M^{z+}]/[G-C18:1], with M^{z+}= Ca^{2+}, Ag^{+}, Al^{3+} and Fe^{2+}, or, when relevant, in the form positive-to-negative charge ratio, [X^{+}]/[G-C18:1], with [X^{+}]= 2[Ca^{2+}], [Ag^{+}], 3[Al^{3+}] or 2[Fe^{2+}], considering that at pH> 8, all G-C18:1 molecules bear a negative charge related to the ionized carboxylic acid.

Cation-resolved and pH-resolved in situ small angle X-ray scattering (SAXS). In situ SAXS experiments are performed at room temperature on the Swing beamline at Soleil Synchrotron (Saint-Aubin, France) during the proposal number N°20201747. The Swing beamline is used

with an energy of E = 12 KeV and a fixed sample-to-detector Eiger X 4M distance of 2.005 m. q is the wave vector ($q = 4\pi/\lambda \sin(\theta)$, 2θ correspond to the scattering angle and λ the wavelength. The q-range is calibrated between $\sim 0.05 < q / nm^{-1} < \sim 5$; raw data obtained on the 2D detector are integrated azimuthally using the in-house software provided at the beamline and thus to obtain the typical scattered intensity I(q) profile. Absolute intensity units are determined by measuring the scattering signal of water ($I(q=0) = 0.0163\ cm^{-1}$). A peristaltic pump is used to ensure a flow through the borosilicate glass capillary (Ø = 1.5 mm) and produce a constant mixing in a vial connected to the capillary and containing the pH electrode.

The volume of the G-C18:1 solution is V= 2 mL, to which the solution containing a given cation is added by mean of a computer-controlled syringe pump available at the beamline. In order to optimize the final cation-to-G-C18:1 ratio within a reasonable experimental time of 20 min to 30 min, specific conditions have been worked out. The concentration of the initial cation solutions for the *in situ* SAXS experiment are: $[Ca^{2+}]$= 140 mM, $[Fe^{2+}]$= 315 mM; $[Al^{3+}]$= 88 mM, while the addition rate is set at 0.163 µL/s for all cation solutions. The concentration of each cation inside the G-C18:1 is precisely calculated by considering the cation's and G-C18:1 initial concentrations, addition rate of the cation's solution, time of addition and dilution factor. The SAXS sampling rate is: acquisition time of 1 s and waiting time between two acquisitions of 10 s. The pH is automatically recorded each 5 s directly inside the vial containing the G-C18:1 solution.

pH monitoring. *In situ* pH monitoring is performed using a Mettler Toledo microelectrode connected to a Hanna scientific pH-meter, model HI 5221. The pH meter is connected to a computer, equipped with the fabricant's software [HI 92000, version 5.0.28].

Rheology. A MCR 302 rheometer (Anton Paar, Graz, Austria) equipped with sand-blasted plate-plate geometry (Ø: 25mm, gap between 0.5 – 1 mm) at a regulated temperature of 25°C is used with a solvent trap with water, so to minimize evaporation. About 0.5 mL of the gel is loaded on the center of the plate using a spatula in order to prevent trapped bubbles. Excess gel is carefully removed.

Cryogenic-transmission electron microscopy (Cryo-TEM). Cryo-TEM for $\{Ag^{+}\}$G-C18:1 and $\{Ca^{2+}\}$G-C18:1 samples was carried out on a FEI Tecnai 120 twin microscope operating at 120 kV with an Orius 1000 CCD numeric camera. Cryo-TEM for $\{Al^{3+}\}$G-C18:1 and $\{Fe^{2+}\}$G-C18:1 samples was carried out on a FEG JEM 2010F microscope operating at 200 kV with a

Gatan Ultrascan 4k CCD numeric camera. For both instruments: the sample holder was a Gatan Cryo holder (Gatan 626DH, Gatan); Digital Micrograph software was used for image acquisition under low dose conditions; cryo-fixation was done with a homemade cryo-fixation device. The solutions were deposited on a glow-discharged holey carbon coated TEM nikel grid (Quantifoil R2/2, Germany). Excess solution was removed and the grid was immediately plunged into liquid ethane at -180°C before transferring it into liquid nitrogen. All grids were kept at liquid nitrogen temperature throughout the entire experimental process. Cryo-TEM images have been treated and analyzed either using Fiji software, available free of charge at the developer's web site,[75] or directly on the Powerpoint™ software.

Turbidimetry. Turbidimetry experiments have been performed using the Malvern Zetasizer Nano ZS 90 (Malvern Instruments Ltd., Worcestershire, United Kingdom) dynamic light scattering instrument. Incident beam is obtained by a 4 mW He−Ne laser at a wavelength λ= 633 nm, at a measuring angle θ = 90°, at room temperature T= 25 °C. The instrument is employed in a static light scattering mode, monitoring the scattered light in kcounts per second (kcps) at a fixed attenuation value set 11 (no attenuation). The scattered light is averaged over 30 s. Before measurement, the G-C18:1 solution ($C_{G\text{-}C18:1}$= 0.5 wt%, pH 8) is filtered with a regenerated cellulose filter of pore size of 0.45 µm (Sartorius). Known, although variable, volumes of the cation solution (0.5 M) are added into a 2 mL G-C18:1 solution. The concentration of the cation inside the G-C18:1 solution is eventually calculated by taking into account the dilution factor. All solutions are vortexed before analysis. The uncertainty over the value of scattered light is estimated by reproducing the experiment in duplicate on the calcium-based system. This uncertainty has been applied to all cations so to estimate the average error.

Results and discussions

Macroscopic transitions, gel structure and its elasticity.

In water at pH 8 and concentrations below 5 wt%, the biosurfactant G-C18:1 mainly forms a micellar phase, possibly coexisting with nanoscale flat objects, due to its negatively charged carboxylate group.[50,51] Below pH 8, a micelle-to-vesicle transition has been previously observed in the absence of added salt.[50,51] If the addition of molar amount of NaCl at pH 8 under diluted G-C18:1 conditions has no specific effect on its phase diagram (Figure 1b), besides screening the charge of the micelles,[55] addition of alkaline earth and transition metal cations trigger a micelle-to-fiber phase transition[54,55] and prompt formation of metallogels for a number of cations.[55,56] In this work, we select to study four different systems, representative of the metallogel behaviour of G-C18:1 found for a number of metal ions.[55] Ca^{2+} and Ag^{+} generate hydrogels composed of self-assembled fibers (Figure 1b) with an analogous crystalline structure and tendency to form β-sheet-like rafts.[54,55] Fe^{2+} and Al^{3+}, on the contrary, form hydrogels with a wormlike micelle structure (Figure 1b).[55] These data are partially summarized in Figure 2, where the corresponding cryo-TEM, SAXS and rheology experiments are presented. Detailed description of the data in Figure 2 can be found in Ref. [54–56].

Cryo-TEM shows the typical structures observed for all (Ca^{2+}, Ag^{+}, Fe^{2+} and Al^{3+}-based) hydrogels (C= 0.5 wt%): {Ca^{2+}}G-C18:1 and {Ag^{+}}G-C18:1 show fibers undergoing side-by-side association,[54] while {Fe^{2+}}G-C18:1 and {Al^{3+}}G-C18:1 are characterized by an interwined network of wormlike micelles (Figure 2a, additional images in Figure S 1).[55]

The typical small-angle X-ray scattering (SAXS) profiles of all metallogels (C= 3 wt%) are shown in Figure 2c, as well as the control G-C18:1 sample liquid solution (spherical micelles) before metal ion addition and labelled Na^{+} (this cation is added during alkalinisation with NaOH). On one hand, the SAXS pattern of {Ca^{2+}}G-C18:1 and {Ag^{+}}G-C18:1, described in more detail in Ref. [54], are compatible with a fibrous morphology, as shown by the diffraction peaks at mid- and high q and the -2 scattering dependency of the intensity at low q. A slope of -2 could be associated to fibers with a flat cross section[9,76] but also to fibers laterally-associated in flat raft-like structures. The diffraction peaks are associated both to the fiber's internal and associative structures. A more detailed study of these materials is given in Ref. [54].

On the other hand, the SAXS profile of {Fe^{2+}}G-C18:1 and {Al^{3+}}G-C18:1 metallogels have low q dependency of the intensity closer to -1.6. This value is typical of wormlike structures,[77,78] due to the analogy between worms and swollen polymer chains.[79,80] The broad oscillation at high q (the meaning of the low-amplitude oscillation in {Al^{3+}}G-C18: at about

1.7 nm^{-1} will be discussed further in this work) is rather compatible with a micellar than a fibrillar morphology.[80]

All SAXS patterns strongly differ from the metal-free, Na^+-containing, system (Figure 2c). In the latter, the broad interaction peak and oscillation below and above 1 nm^{-1}, respectively, are typical of spheroidal micelles undergoing electrostatic repulsive interactions.[80,81] Altogether, the SAXS experiments agree with the cryo-TEM data.

The frequency-dependent storage and elastic moduli of {Ca^{2+}}G-C18:1 and {Fe^{2+}}G-C18:1 hydrogels are shown in Figure 2b, showing the typical hydrogel characteristics for both systems at G-C18:1 concentrations above 1 wt%, as well as the strong impact of pH, the higher, the stronger the hydrogel. At neutral pH, the viscoelastic modulus given by the {Ca^{2+}}G-C18:1 metallogel is not frequency-dependent, thus suggesting a solid-like structure. The low absolute value of G' and G'' suggests the low density of junctions point between structures forming the viscoelastic network. The viscoelastic modulus of the {Fe^{2+}}G-C18:1 metallogel are frequency-dependent, suggesting a liquid-like behavior of the sample. The higher G' compared to Ca^{2+} suggests an higher density of junction point, which could be linked to the higher ratio of [Fe^{2+}]/[G-C18:1] (1.4) compared to [Ca^{2+}]/[G-C18:1] (0.6). Additional data illustrating the elastic properties of the hydrogels, as well as structural considerations and supposed explanation behind the effect of each cation can be found elsewhere.[54–56]

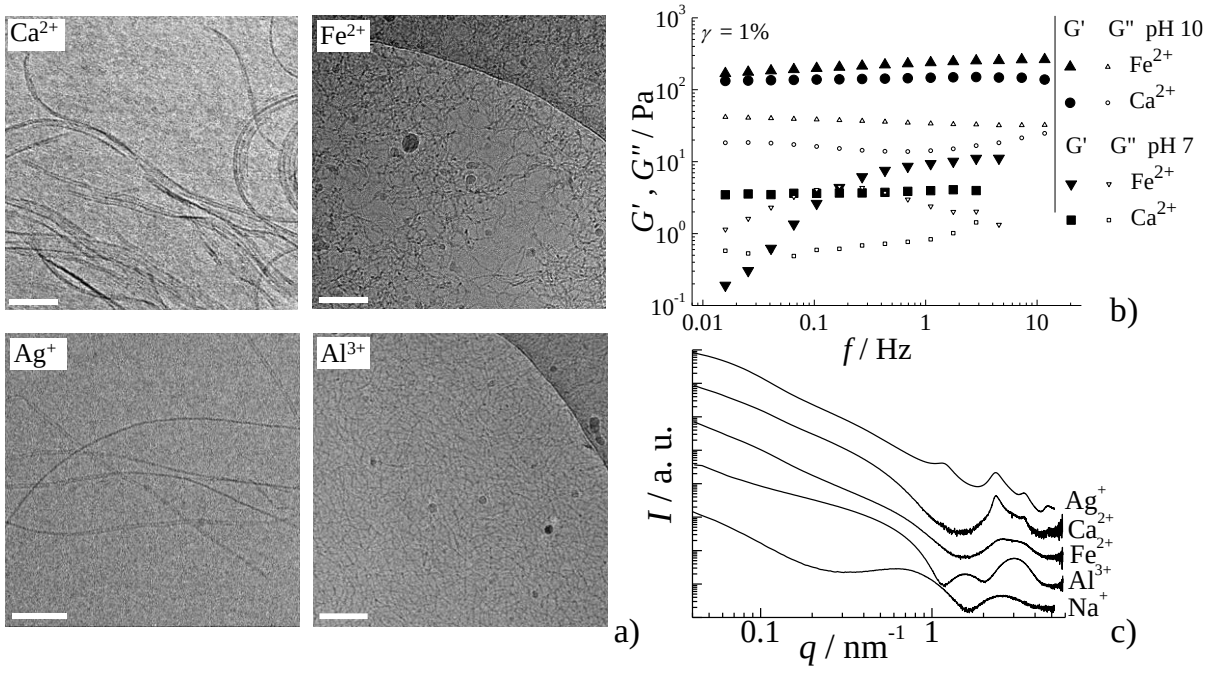

Figure 2 – a) Cryo TEM images of a 0.5 wt% G-C18:1 solution (pH 8) containing Ca^{2+}, Ag^+, Fe^{2+} and Al^{3+} metal ions at a molecular ratio [Ca^{2+}]/[G-C18:1] = 0.6, [Ag^+]/[G-C18:1]= 1, [Fe^{2+}]/[G-C18:1] = 1.4, [Al^{3+}]/[G-C18:1] = 0.34. Scale bar

is 100 nm. Spheroidal aggregates in cryo-TEM images are artefacts due to due cryo-fixation.[82] b) Typical frequency sweep storage (full symbols) and loss (empty symbols) moduli for calcium and iron gels ($C_{G\text{-}C18:1}$= 3 wt%). c) Typical SAXS profiles recorded on G-C18:1 (C= 3 wt%, except for the Ca^{2+}, where C= 0.5 wt%) samples; all samples form metallogels except Na^{+} (liquid solution). All SAXS profiles are reported in Ref. [55].

Di- and trivalent cations have a major impact on the self-assembly and macroscale properties of G-C18:1, as they induce a phase transition and, in many cases, formation of hydrogels. Cation-induces self-assembly on amphiphiles is often observed in the literature; its fundamental aspects have been studied, often from the point of view of chaotropicity,[32] as well as direct applications.[36,46] The complexation of COO^- groups by cations has been often interpreted in terms of the "egg-box structure", especially for Fe^{2+},[83] Ca^{2+}[84] and Ag^+.[85] Al^{3+} has long been studied in relationship to phase transitions in anionic surfactants,[86,87] but other studies show its effect as cross-linker in hydrogels,[88] and interactions with carboxylate group are also described.[89]

In our previous work,[55] which explored a number of alkaline earth and transition metal cations on the self-assembly properties of G-C18:1, it has been proposed that fibrillation and hydrogel formation are favored for those cations, which exist as free ions in solution at the pH of work (between 8 and 10). A deeper insight on the structure of {Ag^+}G-C18:1 and {Ca^{2+}}G-C18:1 fibrous hydrogels, performed by combining cryo-TEM, SAXS, ^{13}C solid-state NMR and isothermal titration calorimetry, suggests the formation of silver-G-C18:1 dimers through COO^--Ag^+ complexation.[54] The role of calcium is less clear, although ITC shows that self-assembly occurs in a two-step process, charge screening and hydrophobic effect at low calcium content and Ca^{2+}-COO^- complexation at high calcium content.[54] On the contrary, micellar hydrogels seem to be favoured by those cations having a more complex speciation (spontaneous hydroxylation of ion in $M_x(OH)_y^{(xz-y)+}$ species, with z being the valence of M^{z+}) in water, for which complexation by the COO^- groups competes with spontaneous hydroxylation.[90,91] The most plausible hypothesis explaining the formation of micellar aggregates is the screening of the negatively-charged micelles by the positively-charged hydroxylated metal ions, and which could induce a morphological transition between spheroidal and elongated micelles. Cation-induced elongation of spheroidal micelles is common for anionic surfactants,[33–35] but speciation is not often considered (refer to Table S 1 in Ref. [55]) and charge neutralization by hydroxylated ions is a hypothesis rarely taken into consideration.[92]

The morphological evolutions of G-C18:1 induced by Ag^+ and Ca^{2+} on one side, and Fe^{2+} and Al^{3+} on the other side, are qualitatively studied by turbidimetry and more deeply by a

series of cation-resolved *in situ* SAXS experiments. For the latter, a specific apparatus, previously used to study pH-resolved morphological transitions amphiphilic systems,[51,74] has been adapted to the present goal. The solution containing G-C18:1 is continuously pumped through the SAXS capillary by mean of a peristaltic pump, while the solution containing the chosen cation is slowly injected in the vial containing the G-C18:1 solution at a constant and optimized rate of 0.163 µL/s. The pH is constantly monitored throughout the process in an automated fashion. All systems are labelled {Al^{3+}}G-C18:1, {Fe^{2+}}G-C18:1 and {Ca^{2+}}G-C18:1. Unfortunately, due to the high (exothermic) reactivity[54] between Ag^{+} and G-C18:1, the {Ag^{+}}G-C18:1 system could not be studied, as addition of silver into the G-C18:1 solution induces the prompt formation of aggregates, which are not dissolved fast enough and either clog the capillary or sediment.

Turbidimetry is a practical experiment, which allows an immediate evaluation of the transition from small (micelles) to large colloids. Figure 3 presents the turbidimetry study of {Al^{3+}}G-C18:1, {Fe^{2+}}G-C18:1 and {Ca^{2+}}G-C18:1 solutions in terms of amount of scattered light as a function of the charge ratio [X^{+}]/[G-C18:1], with [X^{+}] corresponding to the charge molar concentration (mol/L), [X^{+}]≡ 2[Ca^{2+}], 2[Fe^{2+}] and 3[Al^{3+}], and considering that each G-C18:1 carries a carboxylate group at pH= 8.

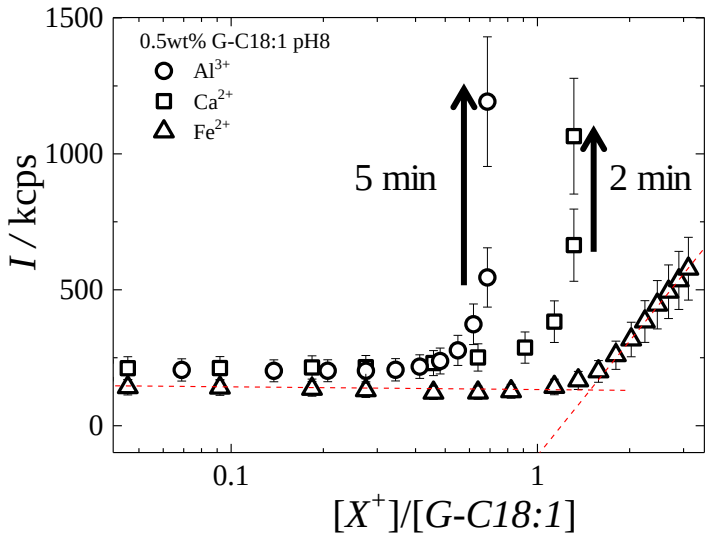

Figure 3 - Average light scattered as a function of the charge ratio [X^{+}]/[G-C18:1]. Arrows represent the increase of light scattered after few minutes at the same charge ratio. Intersection of dash lines correspond to the critical charge ratio of the macroscopic phase transition.

The micellar solution is clear at pH 8 and it produces minimal light scattering, identified by the initial plateau at low charge ratio. The scattered light increases above roughly a charge

ratio of 0.5 for the Ca^{2+} and Al^{3+} systems. Determination of a critical ratio using the method of line intersection is not possible due to the time dependency of the scattered light at a constant ratio. This is illustrated in Figure 3 by the sudden increase in scattered light, marked by the black arrows. A qualitative estimation of the ratio at which phase transition occurs is about 0.6 and 1 for Al^{3+} and Ca^{2+}, respectively. For the iron gel, slopes intersect at a charge ratio of 1.5. An overview of the ratios indicate that phase transition occurs at $[X^+]/[G\text{-}C18:1]= 1\ Al^{3+}$ for ~5 G-C18:1, 1 Ca^{2+} for 2 G-C18:1 and 3 Fe^{2+} for 4 G-C18:1. These values, although qualitative, still suggest that large structures form upon charge neutralization for $\{Ca^{2+}\}$G-C18:1, while this is not the case for iron and aluminium, reinforcing the previously-formulated hypothesis[55] that more than one species, each of different charge, exists in solution for these cations.[90,91] More precise insight are hence obtained by SAXS experiments.

Cation-resolved in situ experiments

Cation-resolved *in situ* SAXS experiments are presented for Ca^{2+} (Figure 4), Fe^{2+} (Figure 5) and Al^{3+} (Figure 6) systems. Before adding the cation, the G-C18:1 (0.5 wt%) is at pH 8 in its micellar phase, similarly as in the turbidimetry experiment. The overall cation-to-G-C18:1 molar ratio is chosen so to explore the same range of values, previously optimized to form a hydrogel at higher G-C18:1 concentrations.[55] The presentation of the data is similar for all cations: typical SAXS profiles exploring the entire cation-to-lipid ratio are presented in the a)-panels, while the fits of the slopes in the *low-q* and *mid-q* ranges are presented in b)-panels. 2D contour plots are occasionally shown in the case a specific system undergoes crystallization. Fitting the log(I) against log(q) profiles reflects a typical model-independent analysis, which informs about shape or the aggregation state of a colloid in solution. Typical values of the slope in the *low-q* range, -1, -2 or -4, are generally associated to well-defined cylindrical, flat morphologies or sharp interface, respectively.[93] Non-integer values are on the contrary associated to mass (1 – 3) or surface (3 – 4) fractals,[94,95] where a value of -4 commonly identifies a smooth surface. Model-dependent analysis could be possible. However, SAXS is an additive technique, meaning that the signal of all species in solution adds up to the final I(q) profile. Considering the coexistence of multiple G-C18:1 morphologies, hydroxylated cations and continuous dynamic evolutions with cation content, we prefer to avoid this analytical strategy, which would require a too large effort considering the high uncertainty in terms of existing morphologies.

The q-regions identified in this work correspond to: 1) *low-q*, $q \leq 0.15$ nm^{-1} (typical distance, $d= 2\pi/q \geq 41$ nm); 2) *mid-q*, $0.15 \leq q / nm^{-1} \leq 1.5$ ($41 \geq d / nm \geq 4.2$); 3) *high-q*, $q \geq$

1.5 nm^{-1} ($d \leq 4.2$ nm). However, for the purpose of this work, we disregard the *high-q* region, as it mainly displays either the oscillation of the form factor or crystalline peaks. Linear fits are then performed only in the *low-q* and *mid-q* ranges. However, since the *mid-q* region shows large variations of the slopes across the experiments, the data are split in two sub regions and two slopes are employed to correctly describe the data. The *mid-q* region is then further split in *mid$^-$-q*, with $0.15 \leq q / nm^{-1} \leq 0.6$ ($40 \geq d / nm \geq 10$) and *mid$^+$-q*, with $0.7 \leq q / nm^{-1} \leq 1.5$ ($10 \geq d / nm \geq 4$).

Previous pH-resolved *in situ* SAXS studies were performed to study the self-assembly of G-C18:1 in water at C= 0.5 wt%, the same concentration used in this work, without adding metal ions, except for Na^+, necessarily introduced during the alkalinisation process with NaOH.[50,51] The G-C18:1 solution at pH> 8 is characterized by the typical scattering profile of spheroidal micelles, to which a *low-q* contribution with a slope close to -2 is superimposed. At pH below 8, the *low-q* contribution becomes more and more relevant and it dominates at pH< 6, while the *mid-q* contribution settles between -1 and -2, typical of wormlike fractals.[77–79]

Combination between SAXS and cryo-TEM demonstrated that the *low-q* contribution could be attributed to poorly defined flat structures at pH> 8 and to flat membranes and vesicles at pH< 8, while the *mid-q* contribution to wormlike micelles, which merge into the flat structure between pH 6 and 7. One should note that for the present work, we did not judge useful to perform a control experiment, in which an aqueous metal-free solution is added to a 0.5 wt% G-C18:1 solution at pH 8. To be comparable with the experimental protocol employed in the cation-resolved *in situ* SAXS presented below, the G-C18:1 solution would experience a simple dilution of less than 5%, which would have no influence at all on the established micellar phase.

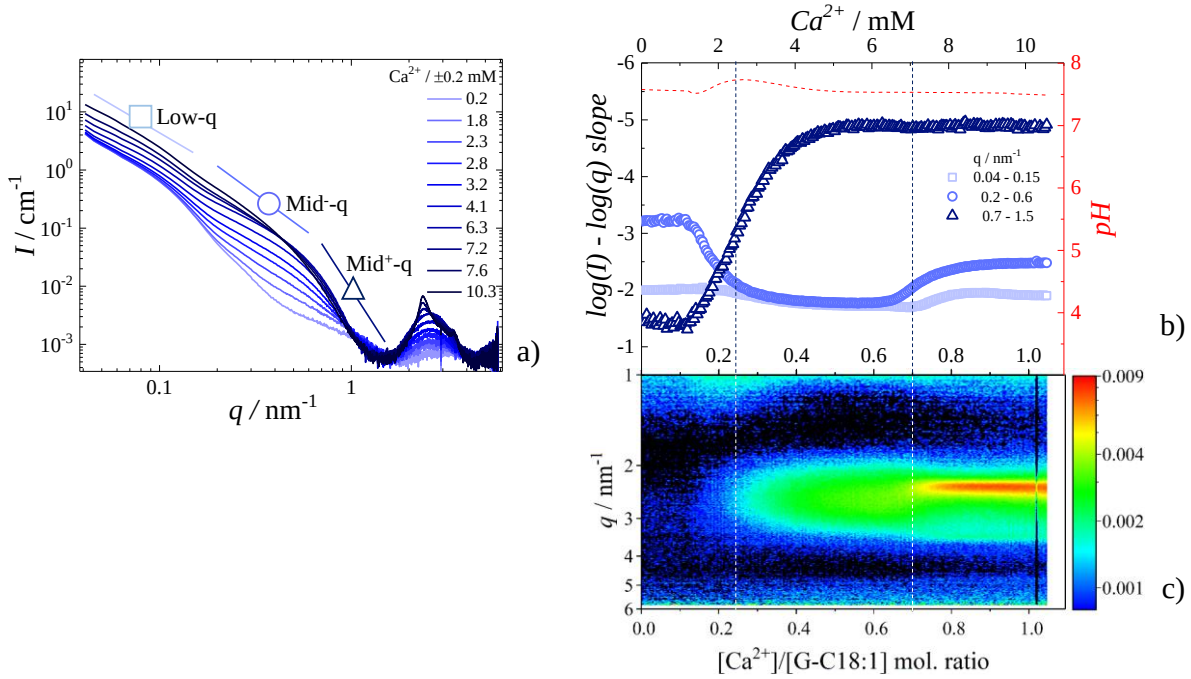

Figure 4 - a) Selected SAXS profiles corresponding to the {Ca^{2+}}G-C18:1 ($C_{G\text{-}C18:1}$= 0.5 wt%) system for different Ca^{2+} concentrations. Each curve corresponds to an average of ten curves, causing an uncertainty on the concentration of about ± 0.2 mM. Solid lines with square, circle and triangle indicate the q-regions fitted by a linear function. b) Slopes corresponding to the fit of the log(I)-log(q) curves in a) as a function of the molar ratio [Ca^{2+}]/[G-C18:1]. Squares, circles and triangles correspond to the *low-q*, *mid*$^{-}$*-q* and *mid*$^{+}$*-q* regions defined in a). The top x-axis indicates the calcium concentration. The right-hand y-axis corresponds to the red dash line giving the pH during calcium addition. c) Contour plot focused on the *high-q* region as a function of the molar ratio [Ca^{2+}]/[G-C18:1].

{Ca^{2+}}G-C18:1. In situ SAXS experiments of {Ca^{2+}}G-C18:1 until a molar ratio of 0.1 show similar features to the ion-free system, with *low-q* slope of -2 (squares, Figure 4) and *mid*$^{+}$*-q* slope of about -1.6 (triangles, Figure 4), and no slope variation. The absence of any structural change is actually in agreement with calorimetry data,[54] showing no heat exchange before 0.1. Interestingly, the *low-q* region exhibits a practically continuous slope of -2 during the entire calcium addition, from molar ratio 0 to 1, while important changes occur in the *mid-q* region above 0.1.

The slope in the *mid*$^{-}$*-q* region evolves from -3.2 at a ratio of 0.1 to -2.0 above a ratio of 0.25 until a ratio 0.7. The slope value in the order of -3, compatible with a surface fractal, is attributed here to the interfacial contribution of the flat objects scattering at *low-q*, and which superimpose to the signal of the micellar aggregates. The evolution towards the -2 slope suggests a massive increase in the amount of flat structures, most likely following continuous morphological transition from micelles, as shown by the increase in slope from -1.4 to - 4.9 in the *mid*$^{+}$*-q* range. The flat structures are attributed to a morphology with flat cross section (Figure 2a, Ca^{2+}).[54]

Above the molar ratio of 0.55, which corresponds to a macroscopic change in turbidimetry (Figure 3), the slope at *mid*$^{+}$*-q* becomes constant and suggests the end of the phase transition from micelles to fibers. This is confirmed by the appearance of the fibers' diffraction peak at q = 2.36 nm^{-1} (d= 2.66 nm) above the ratio of 0.7, thus showing that intra-fiber crystallization occurs at a later stage in the process of fiber formation. The peak has been largely discussed in previous work[54] and possibly attributed to an oblique lattice within the fiber's plane.

The critical molar ratio of 0.25 and 0.7 are shown by vertical dash lines in Figure 4c so to define the onset of the micelle to fiber transition and the intra-fiber crystallization, respectively. One should also note that the pH is practically constant at the value of 7.5 during the entire experiment, showing that no spurious acido-base activity, neither concerning the COO^- nor Ca^{2+}, takes place. This is expected, as from the well-known speciation of calcium, hydroxylation only occurs at highly alkaline pH, generally above 11.[90]

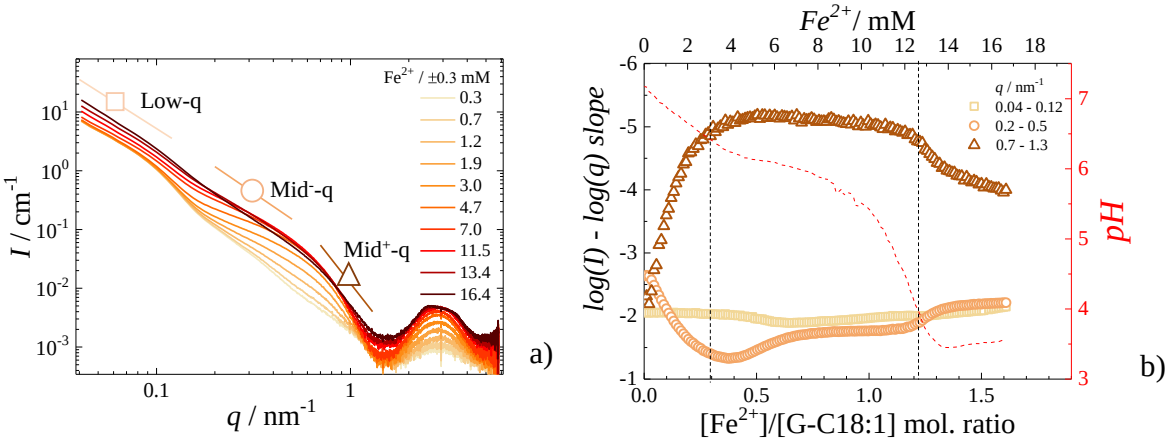

Figure 5 – Selected SAXS profiles corresponding to the {Fe^{2+}}G-C18:1 ($C_{G\text{-}C18:1}$= 0.5 wt%) system for different Fe^{2+} concentrations. Each curve corresponds to an average of ten curves, causing an uncertainty on the concentration of about ± 0.3 mM. Solid lines with square, circle and triangle indicate the q-regions fitted by a linear function. b) Slopes corresponding to the fit of the log(I)-log(q) curves in a) as a function of the molar ratio [Fe^{2+}]/[G-C18:1]. Squares, circles and triangles correspond to the *low-q*, *mid*$^{-}$*-q* and *mid*$^{+}$*-q* regions defined in a). The top x-axis indicates the iron concentration. The right-hand y-axis corresponds to the red dash line giving the pH during iron addition.

{Fe^{2+}}G-C18:1. The addition of Fe^{2+} to G-C18:1 shows similar trends as in {Ca^{2+}}G-C18:1 in terms of the evolution of the slopes with molar ratio, except the fact that the reaction seems faster with iron and crystallization does not occur (Figure 5). The drop in pH and prompt slope evolution in the *mid-q* range as soon as iron is added demonstrate faster reactivity, while absence of diffraction peaks is a sign that crystallization does not occur. Besides these facts, the slopes evolve in a similar direction up to the ratio of 0.3: the *low-q* contribution (squares, Figure 5) starts and stay at -2, as for calcium; the *mid*$^{-}$*-q* contribution (circles, Figure 5) decreases from

about -2.7 to -1.3, while the *mid*$^{+}$*-q* (triangles, Figure 5) promptly increases from about -2 to -5. From the ratio 0.3 to 1.2, SAXS spectra do not show large variations, except for the pH decrease from 6.2 to 4.6 and a slight evolution of the *mid*$^{-}$*-q* towards about -1.7/-1.8. If the *low-q* contribution always suggests the presence of flat structures, of which the nature is less defined in this system, the evolution of the signal in the *mid-q* region (*mid*$^{-}$*-q* and *mid*$^{+}$*-q*) confirms the hypothesis of aggregated wormlike objects, as observed by cryo-TEM (Figure 2a, Fe^{2+} and Figure S 1). The oscillation of the form factor at *high-q* is sensitive to the electron density contrast at the interface between water and the scattering object, the larger the amplitude, the higher the contrast. The increase in the amplitude of the oscillation of the form factor for *{Fe*$^{2+}$*}G-C18:1* confirms important changes in the contrast, which can be explained by both a morphological change and a progressive adsorption of cations, which have a strong electron density contrast with respect to water and G-C18:1. Further addition of iron up to molar ratio above 1.5 shows additional changes: the *low-q* and *mid*$^{-}$*-q* regions achieve a -2 slope, the *high-q* background level increases and the form factor oscillation becomes unsymmetrical, possibly hiding broad correlation peak at 2.5 nm^{-1}. These changes could signify either further morphological evolution or aggregation. However, in the absence of complementary data, one cannot make a clear-cut statement.

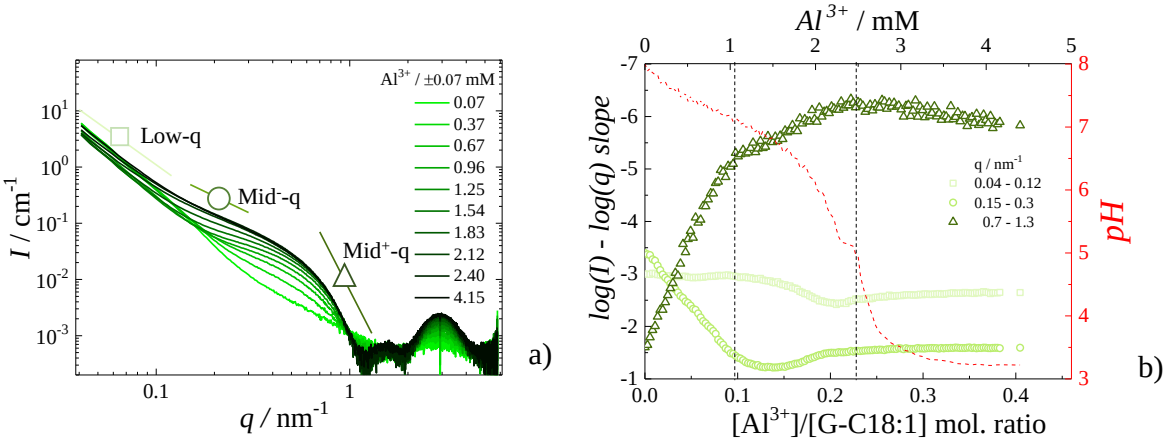

Figure 6 - Selected SAXS profiles corresponding to the {Al^{3+}}G-C18:1 ($C_{G\text{-}C18:1}$= 0.5 wt%) system for different Al^{3+} concentrations. Each curve corresponds to an average of ten curves, causing an uncertainty on the concentration of about ± 0.07 mM. Solid lines with square, circle and triangle indicate the q-regions fitted by a linear function. b) Slopes corresponding to the fit of the log(I)-log(q) curves in a) as a function of the molar ratio [Al^{3+}]/[G-C18:1]. Squares, circles and triangles correspond to the *low-q*, *mid*$^{-}$*-q* and *mid*$^{+}$*-q* regions defined in a). The top x-axis indicates the aluminium concentration. The right-hand y-axis corresponds to the red dash line giving the pH during aluminium addition.

{Al^{3+}*}G-C18:1.* The molar ratio dependency of the SAXS data for Al^{3+} (Figure 6) is somewhat similar to the trends found for Fe^{2+} until a ratio of 0.1: the *low-q* slope is constant at about -3, the *mid*$^{-}$*-q* slope drops from -3 to about -1 while the *mid*$^{+}$*-q* slope increases from -1.5 to -5. In

the absence of diffraction peaks, as for iron, such variations indicate an evolution towards elongated, possibly aggregated, wormlike objects. Between the ratio 0.1 and 0.23 the *low-q* slope evolves towards -1.5, the *mid$^-$-q* slope stabilizes between -1.3 and -1.5, typical of wormlike aggregates[77–79] for the analogy between polymer chains and worms,[79,80] while the *mid$^+$-q* slope evolves towards values of -6. Such a high slope should be interpreted as the achievement of an interface (which, for smooth interfaces, display a -4 dependency over a larger q-range[79]). Above the ratio 0.23, these values do not evolve any longer, but the *high-q* region is characterized by an odd oscillation centered at 1.5 nm^{-1}, besides the oscillation centered at 3 nm^{-1} found for the calcium and iron systems. Vertical dash lines have been added to Figure 6b to better visualise the limits of the phase transitions.

If part of the SAXS data are compatible with a network of elongated, condensed, micelles, as for the iron system and in agreement with cryo-TEM (Figure 2a, Al^{3+}, Figure S 1), the oscillation centered at about 1.5 nm^{-1} strongly suggests the presence of a second species, coexisting with the assembled form of G-C18:1. The first, probably obvious, hypothesis could involve the coexistence of two forms of self-assembled G-C18:1. However, out of all alkaline earth and transition metal salts tested in combination with G-C18:1, only the SAXS profile of {Al^{3+}}G-C18:1 displays such an additional oscillation,[55] which appears for [Al^{3+}]> ≈1.2 mM (Figure 6a), corresponding to pH< 7 (Figure 6b). It would be uncomfortable to explain the reason why only aluminium would induce a second G-C18:1 structure. Furthermore, Al^{3+}-induced phase transitions in anionic surfactants do not show specific features, besides sphere -to-rod,[33–35] -to-wormlike[37,96] or –to-vesicle[97] transitions. The second hypothesis could then involve aluminium itself.

As widely known in the literature, at acidic pH aluminium has a strong tendency to self-associate into aqueous clusters involving from 2 to 54 aluminium atoms and of which the most important is known as “Keggin cluster”, composed of 13 atoms of aluminium, often referred to as Al_{13}.[90,98] The Keggin cluster forms at below pH 6, a range of pH compatible with the pH reached in G-C18:1 solutions at high Al^{3+} content: the pH drops from 8 to 3.3 from the aluminium-free to the ratio of 0.3 (Figure 6b, right-hand side). However, the typical radius of the Keggin cluster is about 1.26 nm,[99] which is not compatible with an oscillation centered at 1.5 nm^{-1}. SAXS data collected on aluminium clusters show that the oscillation should be more centered at about a decade higher.[100] An oscillation centered at 1.5 nm^{-1} could only be accounted for a colloid having an equivalent radius at least 2.5 times higher. The qualitative fit of the oscillation at 1.5 nm^{-1} ([Al^{3+}]= 4.15 mM) indicates a colloid, arbitrarily taken as spherical, having a diameter of 3.9 nm (Figure S 2). Aluminium oxopolymers can however be found in

various shapes (particles, platelets)[98,99] and size,[98] in particular between pH 7 and pH 4,[98] meaning that aluminium oxocluster larger than the Keggin could be compatible with an oscillation at 1.5 nm^{-1}. If further experiments, such as solid state NMR, classically employed to study aluminium oxoclusters,[98] should be employed to verify this hypothesis, which is out of the scope of this work, the hypothesis of aluminium oxoclusters is privileged over other forms of self-assembled G-C18:1 structures.

Phase transition by Ca^{2+} addition.

In situ SAXS data (Figure 4) related to the addition of Ca^{2+} show a continuous micelle-to-fiber phase transition. The presence of fibrous ribbons is confirmed by cryo-TEM and corroborated by the -2 slope observed in the *low-q* and mid-q regions of the SAXS spectra, in agreement with other works on nanobelts[101] and glycolipid biosurfactants.[9] The initial steps of the transition mainly involve the formation of fibers having an amorphous structure. Fibers crystallize only at ratio ≥ 0.7, as testified by the appearance of the crystalline peak at 2.36 nm^{-1}, previously attributed to the (0,1) reflection of an oblique lattice, most likely contained in the ribbon's plane.[54] Interestingly, crystallization occurs at the $[Ca^{2+}]$/[G-C18:1] ratio of 0.7, almost a factor 3 higher than the ratio at which fibers form (0.25), but also higher than the ratio ($[X^+]$/[G-C18:1]= 1, equivalent to $[Ca^{2+}]$/[G-C18:1]= 0.5) at which the macroscopic phase separation becomes relevant in turbidimetric experiments (Figure 3). We believe that the difference between the fiber growth and internal crystallization is most likely due to a slow kinetic process rather than a specific molar ratio. This is put in evidence by complementary SAXS experiments performed at different synthesis times: the structure peak can be easily observed at the same, low, molar ratio but at longer mixing time of calcium and G-C18:1 (Figure S 3).

SAFiN obtained by Ca^{2+} are well-known and generally attributed to bridging and charge screening.[102,103] According to *in situ* SAXS experiments, micelles evolve towards fibrous ribbons at a charge ratio well below 1 and of which the crystallinity is a kinetically-controlled process (Figure S 3). The central role of the carboxylate-calcium interaction is out of doubt. Control experiments show that excess of sodium does not destabilize the micellar phase,[55] while Mg^{2+} produces a liquid-liquid phase separation (not shown). Additionally, a SAFiN gel only forms when calcium is added to the micellar phase (Figure 2a, Ca^{2+}), while a precipitate forms when Ca^{2+} is added to the vesicles phase at pH < 7 and containing a lower content of carboxylate groups.[56]

Despite the carboxylate-calcium interaction, the scheme of the driving forces seems to be more complex. According to the packing parameter theory,[104,105] charge screening in micelles reduces the effective surface area of the polar headgroup, resulting in a lower curvature structure, such as tubes or wormlike micelles,[80] commonly found for surfactant-cation mixtures.[33–35,37,96] For this reason, charge screening arguments alone cannot explain the micelle-to-fiber transition. In fact, addition of Ca^{2+} ions to other biosurfactants having similar structures, namely C18:1 sophorolipids[57] and rhamnolipids,[63] does not produce any remarkable effects besides screening intermicellar repulsive interactions. Concerning the micelle-to-fiber transitions, these have mainly been observed upon neutralization for a number other glycolipid biosurfactants. In particular, an abrupt phenomenon occurs for C18:0 sophorolipids[51] while a continuous one is observed for palmitic C16:0 sophorolipids.[10] The biosurfactant and/or glycolipid nature of the molecule is not a sufficient condition to observe fibrillation, as neither rhamnolipids[63,65] nor surfactin,[64] two common biosurfactants, do not display such property when mixed with mono and divalent alkali earth and transition metal cations. All in all, G-C18:1 has a unique phase behaviour, as outlined elsewhere.[66]

The smooth Ca^{2+}-induced fibrillation of G-C18:1 recalls the continuous micelle-to-fiber transition found for palmitic acid sophorolipids when the pH is acidified.[10] Nevertheless, neutralization of the carboxylate group of G-C18:1 by acidificaiton of the micellar phase actually leads to a vesicle or lamellar phase.[50,51] Calcium must then play a more significant, structural, role very specific to G-C18:1, even at low ion-to-lipid ratio. Calorimetry experiments performed on {Ca^{2+}}G-C18:1[54] show a two-step mechanism, a non-specific endothermic (hydrophobic effect, release of water) process ($\Delta H = +6$ kJ/mol) in the low [Ca^{2+}]/[G-C18:1] regime, below 0.3, and a specific exothermic (ion binding, long-range electrostatic, H-bonding, ion-mediated cross-linking) process above 0.3 ($\Delta H = -11.2$ kJ/mol). These data match well the calcium-resolved *in situ* SAXS (Figure 4b), according to which the micelle-to-fiber transition occurs at ratio below 0.3, while fiber growth, crystallization and multimerization[54] occurs above 0.3.

The most important non-specific endothermic process involved in the self-assembly of amphiphiles is generally related to the entropic gain associated to the release of water molecules. The sources behind this phenomenon are multifold. The most important one is probably the well-known hydrophobic effect, known to drive the self assembly of amphiphiles or polymers,[106–108] and actually observed for the interaction between G-C18:1 and polylysine.[109] However, a number of other phenomena are known to be endothermic, such as dehydration due to ion exchange (e.g., Na^{+} against Ca^{2+}),[107] the weak binding of Ca^{2+} to lipid vesicles,[110] micelle-

to-rod morphological transitions[111,112] and micellization of zwitterionic surfactants.[106] On the other hand, exothermic process are generally associated to specific interactions, some of which could characterize the self-assembly of {Ca^{2+}}G-C18:1: ligand-ion binding (e.g., Ca^{2+}-EDTA),[113] formation of ordered "egg-box" structures in pectin or alginate systems,[85,114] micelle-to-rod morphological transitions[115] and micellization of cationic surfactants.[106]

In the absence of additional data, one can safely state that the initial micelle-to-fiber transition in {Ca^{2+}}G-C18:1 is certainly driven by release of water molecules associate to two possibly coexisting processes, sodium-calcium ion exchange[107] and the hydrophobic effect related to the structural rearrangement of the fatty acid tails. The latter is driven by the need of two G-C18:1 molecules to interact and neutralize one Ca^{2+}, as illustrated by a combination of ^{13}C solid-state NMR and calorimetry.[54] The second exothermic step associated to fiber growth and crystallization is most likely related to a ligand-ion binding[107,113] driven by the proximity between COO^- and Ca^{2+} inside, but also, across the fibers, in analogy to the "egg-box" structures.[85,114] Cryo-TEM (Figure 2a, Ca^{2+}) and SAXS show that {Ca^{2+}}G-C18:1, unlike low-molecular weight gelators based on SAFiN, is able to form ordered β-sheet-like raft domains.[54] It must be believed that the strong bidentate binding of carboxylate to calcium combined to the specific coordination geometry of the latter[116] and packing constraints of G-C18:1 drive the fibers' crystallization process. Interestingly, the twist along the fibers is much less obvious to observe in {Ca^{2+}}G-C18:1 than in ribbons prepared from acidic sophorolipids.[9,10,12,117] This indicates that the twist of the sophorolipid ribbons can be explained by the bulkiness of the sophorose group compared to the glucose group in G-C18:1, and not by stereochemical arguments. Considerations on the chirality in self-assembled fibers can be found elsewhere.[118]

Finally, it is interesting to note that Ag^+-induced fibrillation in {Ag^+}G-C18:1 is fast (*in situ* SAXS is not possible) and much more exothermic[54] than for {Ca^{2+}}G-C18:1, with no enthalpic contribution. This fact was interpreted as a prompt dimerization of G-C18:1 induced by a strong metal-ligand interaction,[119] supported by ^{13}C solid-state NMR arguments[54] and which was previously reported for stearic acid silver complexes.[120]

pH deserves a specific note. *In situ* monitoring shows that pH is practically constant over the entire range of molar ratio (Figure 4). This can be explained by the fact that Ca^{2+} (or Ag^+) ions exist as free ions below pH 10, and they do not undergo acido-base reactions, as otherwise found for transition metal ions.[90] The carboxylate group of G-C18:1 can immediately interact with Ca^{2+} (or Ag^+). Nevertheless, pH may lower at longer reaction times, thus not excluding a coordination of the metal ion by the free hydroxyl groups in solution. Addressing this question is out of the scope of this work.

Phase transition by Fe^{2+} and Al^{3+} addition.

Addition of Al^{3+} or Fe^{2+} sources drives a unique phase transition, from the micellar phase to what reasonably seems to be an intertwined network of elongated micelles, according to cryo-TEM (Figure 2a and Figure S 1) and *in situ* SAXS (Figure 5 and Figure 6). The phase transition starts upon immediate addition of the cations, which produce continuous changes in the slopes at *low-q*/mid-q but also in the oscillation of the form factor at *high-q* of the scattering profiles of SAXS experiments. The limits of the phase transitions, marked by vertical dash lines in Figure 5 and Figure 6, are set at ion-to-lipid ratio of approximately 0.3/1.2 and 0.1/0.23 for Fe^{2+} and Al^{3+} systems, respectively. If compared to the Ca^{2+} system, one observes that the experimental charge ratios are somewhat underestimated for both Fe^{2+} and Al^{3+}. From mere charge compensation arguments, one would expect transitions at around 0.5 for Fe^{2+} and above 0.3 for Al^{3+}. Such discrepancies could be explained by a number of concomitant factors, making these systems more complex than Ca^{2+} and Ag^{+}.

During the addition of Al^{3+} or Fe^{2+}, the solution undergoes acidification, from an initial pH of about 8 to a final pH of about 3.5. Lowering of pH has two concomitant effects: neutralization of carboxylate groups and change in the cations' speciation in solution. Neutralization of the carboxylate group has two important consequences. The first one consists in reducing the number of carboxylate groups, thus reducing the number of G-C18:1 molecules involved in the metal-ligand reaction. This fact modifies the expected ion-to-lipid ratio, which is calculated on the assumption that all COOH of G-C18:1 are in the carboxylate form. A second effect may occur on the self-assembly of G-C18:1, known to undergo a micelle-to-vesicle transition at pH below 7 in the absence of salts.[50,51]

Variations in the speciation of the cation have a dramatic effects on both the chemical nature of the ion in solution but also on its charge. Lowering the pH generally favours a plethora of positively-charged species. The speciation diagram of Al^{3+} shows that $Al(OH)_3$, $AlOH^{2+}$, $Al(OH)_2^{+}$ but also a number of charged clusters can coexist at pH below 7.[90,98] Possible existence of large aluminium clusters seems to be confirmed by the appearance of an unexpected pre-oscillation of the form factor, discussed above. On the other hand, if the speciation of Fe^{2+} shows that free ion species are expected at pH below 8, one must compel with the instability and spontaneous oxidation of Fe^{2+} into Fe^{3+}, an event which occurs rapidly under air. This is confirmed by the changes in color from green to brown-dark brown in both solution and gel.[55] In this regard, the speciation of Fe^{3+} is much richer than for Fe^{2+}: $Fe_3(OH)_4$, $FeOH^{2+}$ or $Fe(OH)_2^{+}$ are all stable species below pH 7.[90]

From a structural point of view, both Fe^{2+} and Al^{3+} induce a continuous transition from free micelles to an intertwined network of giant micelles, which is coherent with the number of studies showing the effect of aluminium and iron on the elongation of anionic surfactant micelles.[33–35,86,87,92] The strong increase in the amplitude of the *high-q* oscillation attributed to the form factor generally suggests a change in morphology and a stronger contrast. Both are most likely induced by the interaction between G-C18:1 and the cations. Nonetheless, the mechanism of interaction seems to be different if compared to Ca^{2+} or Ag^{+}, discussed above.

If both Fe^{2+} and Al^{3+} were supposed to play a cross-linking role in other systems,[121,122] the limited content of free ion species exclude an interaction merely based on ligand-ion complexation, as for silver or as widely reported for Ca^{2+} in the presence of some biopolymers (the "egg-box"model).[83] Possible sources of interaction could be of electrostatic origin (charge screening),[40] although between G-C18:1 and any of the charged complex species of Fe^{2+} and Al^{3+}. Indeed, we did observe that most cations displaying a complex speciation induce the formation of intertwined micellar systems of G-C18:1.[55] However, other phenomena based of different hydration of the cations[123] or mixed complexation by the carbonyl ligand and water should not be excluded.[119] Unfortunately, the literature provides a limited amount of data on this topic. If a large body of work does discuss the interactions between surfactants, and amphiphiles in general, with metal ions, very few of them consider speciation (refer to Table S 1 in Ref. [55] for a broader literature survey) and we could only find one system in which possible electrostatic interactions between the surfactant and $Fe(OH)^{2+}$ are potentially evoked.[92] It seems that a lot of fundamental work must still be done to better understand the interactions between amphiphiles and metal-hydroxo complexes in aqueous solutions.

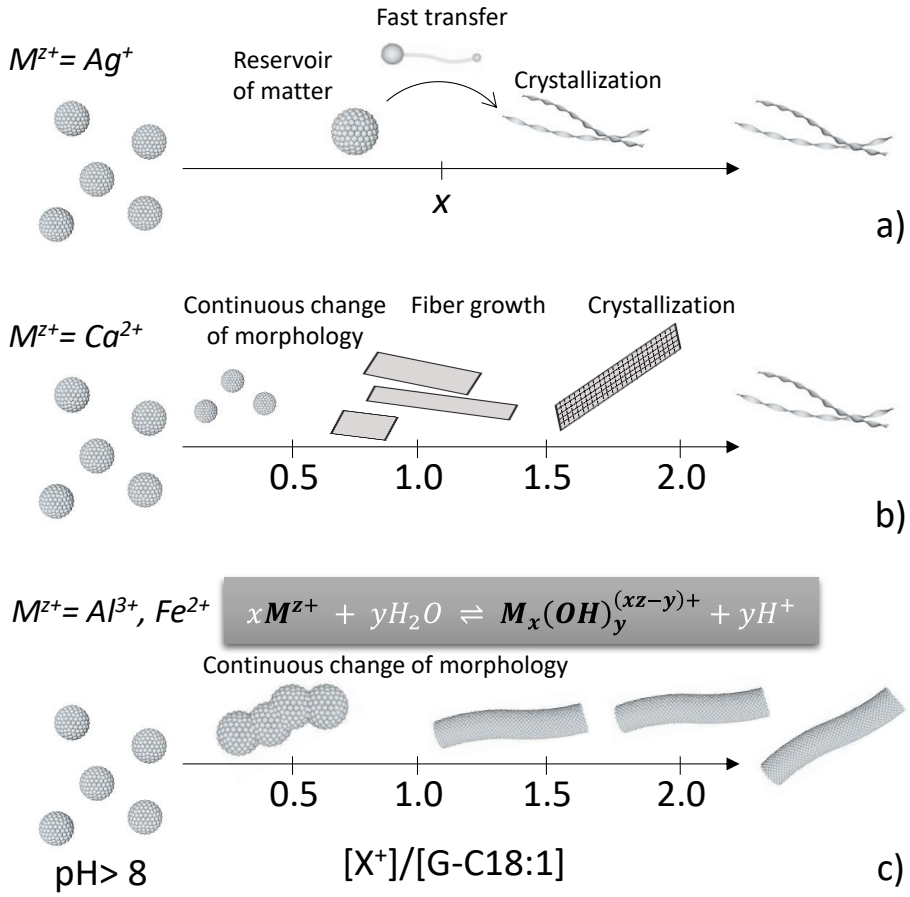

Figure 7 – Summary of the mechanism of self-assembly of G-C18:1 in water (C= 0.5 wt%, ambient temperature) in presence of a) Ag^+, b) Ca^{2+} and c) Al^{3+}, Fe^{3+} metal ions. In c), one must also consider the pH variation and presence of hydroxo metal species, $M_x(OH)_y^{(xz-y)+}$ (z is the valence of M^{z+}) due to the hydrolysis of the cations at pH below 8. According to the speciation diagram, Ag^+ and Ca^{2+} are in the form of free metal ions at pH below 8.[90]

Note on kinetics.

The role of the kinetics and rate of pH variation should not be neglected, either, especially for those cations with a strong acido-base character. Metal ions react with water according to the expression

$$xM^{z+} + yH_2O \rightleftharpoons M_x(OH)_y^{(xz-y)+} + yH^+$$

with z being the valence. The domain of stability of the free metal ions and hydroxo metal species obviously depends on pH and type of metal.[90] The known speciation diagram in water of Ca^{2+} and Ag^+ ions guarantees the free ion, M^{z+}, form below pH 10, a condition which is met in this work: Ca^{2+} and Ag^+ do not form hydroxo species, although they can be still complexed

by water molecules and carboxylate anions of G-C18:1,[119] as discussed in more detailed elsewhere.[54] In particular, ^{13}C solid-state NMR experiments provide a direct proof of the metal-COO^- interaction.[54,66] The kinetics of fiber formation then only depends on the complexation reaction.

On the other hand, Al^{3+} and Fe^{2+}, as well as all other transition metal ions discussed elsewhere,[55] have a pronounced acido-base character, with complex speciation in water in the pH range between 3 and 10, along with possible oxidation of Fe^{2+} into Fe^{3+}.[55] When the pH of the solution becomes more acidic due to the addition of the metal to the G-C18:1 water solution, the outcome depends on the relative acido-base kinetics of the metal and G-C18:1 and the effective rate of pH change. If the acido-base reaction of G-C18:1 is slow (compared to the metal), the metal-induced phase transition towards wormlike micelles and gelification can then occur before the competitive micelle-to-vesicle transition, classically observed upon acidification in the absence of metal ions.[50,51] The content of COO^- may then still be important even at a formally acidic pH. This seems to be the case for gels containing Al^{3+} or Fe^{2+}: the *in situ* experiments (Figure 5 and Figure 6) show that the sphere-to-wormlike transition essentially occurs when the pH is still above 6 and that worms are stable below this pH, where vesicles are otherwise formed in the absence of metal ions.[50,51]

On the other hand, if the acido-base reaction of G-C18:1 is fast, there will not be enough carboxylates to interact with the metal species during acidification, and gelification does not occur. pH must then be increased, as experimentally found for Co^{2+} or Cr^{2+}.[55] It is not excluded that this process is influenced by the rate of addition of the metal ion solution, in analogy to the impact of the rate of pH variation during the gelification process of sophorolipids.[11] Further work is certainly needed to better understand and control the gelification of G-C18:1.

Conclusions

Microbial glucolipid G-C18:1 forms a micellar and vesicular phase at alkaline and acidic pH, respectively. In the micellar phase at pH 8 and above, G-C18:1 undergoes fibrillation and prompt hydrogelation when alkaline earth or transition metal ions are introduced in solution (Figure 1b). At lipid concentration above 1 wt%, Ca^{2+} and Ag^+ drive the formation of SAFiN hydrogels, while Fe^{2+} and Al^{3+} induce the formation of a micellar gel. The cation-resolved *in situ* synchrotron SAXS experiments performed in this work explore the low concentration regime, below 1 wt%, with the goal of better understanding the mechanism behind the phase transitions.

The interaction between Ag^{+} and G-C18:1 is so fast and exothermic that any attempt to perform *in situ* experiments was vain. However, data published elsewhere suggest a strong specific, most likely metal-ligand, interaction between them. The immediacy of the reaction actually suggests that G-C18:1 micelles act as a reservoir of matter before their assembly into fibers (Figure 7a). On the other hand, Ca^{2+} shows a two-step interaction with G-C18:1. Micelles are stable at very low calcium-to-lipid molar ratio (<0.1), they change morphology into fibers between 0.1 and 0.3 and, eventually, they grow and crystallize above 0.3 (Figure 7b). Complementary calorimetry experiments and study on hydrogel formation confirm these assumptions and suggest a charge-neutralization process at low ratio, followed by calcium-carboxylate complexation, massive fibrillation and hydrogelation in the ratio order of 0.5, that is when the negative charge of two carboxylate groups is balanced by a calcium ion.

The interaction between Fe^{2+} and Al^{3+} is somewhat different and it produces a different morphological evolution. Micelles, initially spheroidal, elongate and grow following a power law in the logarithmic representation of the SAXS profiles between -1 and -1.6. This is typical for elongated, wormlike, morphologies similar to swollen polymer chains,[77–79] rather than fibers. The immediate evolution of the SAXS profiles indicates a rapid interaction. The evolution is continuous, compatible with smooth morphological evolution (Figure 7c). The driving force seems to be more related to a charge-screening effect, possibly involving a partial coordination of the metal center by the carboxylate group of G-C18:1. However, the mechanism could be more complex and beyond the possibilities of SAXS. In fact, the important pH drop during the addition of the metal ions reduce the carboxylate content in favour of the carboxylic group. This could have an impact on both the G-C18:1 morphology and on the coordination of the metal ions. Meanwhile, drop in pH has critical consequences on the actual $M_x(OH)_y^{(xz-y)+}$ species (with z being the valence of M^{z+}) in solution (Figure 7c), which are constituted by free Al^{3+} and Fe^{2+} ions, as expected for silver and calcium, but rather on a complex mixture of partially-charged metal-hydroxo complexes or, worst, colloidally polyoxo metal clusters in the case of Al^{3+}, as suggested by a more complex SAXS signal in the *high-q* range.

Acknowledgements

We thank Dr. S. Roelants at Gent University and Bio Base Europe Pilot Plant, Gent, Belgium for dealing with and shipping the G-C18:1 glycolipid. Authors kindly acknowledge the French ANR, Project N° SELFAMPHI - 19-CE43-0012-01. Soleil synchrotron is acknowledged for financial support during the beamtime associated to the proposal number N°20201747. We are

highly grateful to Amélie Leforestier et Jeril Degrouard (LPS, Saclay University) and Labex PALM (ANR-10-LABX-0039-PALM) for the cryo-TEM experiments on the 200 kV Jeol instrument and METSA (METSA Federation, FR3507 CNRS) for financial support.

Supporting Information

Figure S 1 presents additional cryo TEM images of a G-C18:1 solution (pH 8) containing Fe^{2+} and Al^{3+} metal ions. Figure S 2 shows the fit of a typical SAXS profile corresponding to the {Al^{3+}}G-C18:1 system. Figure S 3 shows the SAXS spectra of {Ca^{2+}}G-C18:1 solution at different preparation time.

References

(1) Farias, C. B. B.; Almeida, F. C. G.; Silva, I. A.; Souza, T. C.; Meira, H. M.; Soares da Silva, R. de C. F.; Luna, J. M.; Santos, V. A.; Converti, A.; Banat, I. M.; et al. Production of Green Surfactants: Market Prospects. *Electron. J. Biotechnol.* **2021**, *51*, 28–39.

(2) Markande, A. R.; Patel, D.; Varjani, S. A Review on Biosurfactants: Properties, Applications and Current Developments. *Bioresour. Technol.* **2021**, *330*, 124963.

(3) Lang, S. Biological Amphiphiles (Microbial Biosurfactants). *Curr. Opin. Colloid Interface Sci.* **2002**, *7*, 12–20.

(4) Desai, J. D.; Banat, I. M. Microbial Production of Surfactants and Their Commercial Potential. *Microbiol. Mol. Biol. Rev.* **1997**, *61*, 47–64.

(5) Celligoi, M. A. P. C.; Silveira, V. A. I.; Hipólito, A.; Caretta, T. O.; Baldo, C. Sophorolipids: A Review on Production and Perspectives of Application in Agriculture. *Spanish J. Agric. Res.* **2020**, *18*, 1–10.

(6) Moldes, A. B.; Rodríguez-López, L.; Rincón-Fontán, M.; López-Prieto, A.; Vecino, X.; Cruz, J. M. Synthetic and Bio-Derived Surfactants versus Microbial Biosurfactants in the Cosmetic Industry: An Overview. *Int. J. Mol. Sci.* **2021**, *22*, 2371.

(7) Ribeiro, B. G.; Guerra, J. M. C.; Sarubbo, L. A. Biosurfactants: Production and Application Prospects in the Food Industry. *Biotechnol. Prog.* **2020**, *36*, 1–16.

(8) Baccile, N.; Seyrig, C.; Poirier, A.; Castro, S. A.; Roelants, S. L. K. W.; Abel, S. Self-Assembly, Interfacial Properties, Interactions with Macromolecules and Molecular Modelling and Simulation of Microbial Bio-Based Amphiphiles (Biosurfactants). A Tutorial Review. *Green Chem.* **2021**, *23*, 3842–3944.

(9) Cuvier, A.-S. S.; Berton, J.; Stevens, C. V; Fadda, G. C.; Babonneau, F.; Van Bogaert, I. N. A. a; Soetaert, W.; Pehau-Arnaudet, G.; Baccile, N. PH-Triggered Formation of Nanoribbons from Yeast-Derived Glycolipid Biosurfactants. *Soft Matter* **2014**, *10*, 3950–3959.

(10) Baccile, N.; Messaoud, G. Ben; Griel, P. Le; Cowieson, N.; Perez, J.; Geys, R.; Graeve, M. De;

Roelants, S. L. K. W.; Soetaert, W. Palmitic Acid Sophorolipid Biosurfactant: From Self-Assembled Fibrillar Network (SAFiN) To Hydrogels with Fast Recovery. *Philos. Trans. A* **2021**, *379*, 20200343.

(11) Ben Messaoud, G.; Le Griel, P.; Hermida-Merino, D.; Roelants, S. L. K. W.; Soetaert, W.; Stevens, C. V.; Baccile, N. PH-Controlled Self-Assembled Fibrillar Network (SAFiN) Hydrogels: Evidence of a Kinetic Control of the Mechanical Properties. *Chem. Mater.* **2019**, *31*, 4817–4830.

(12) Baccile, N.; Renterghem, L. Van; Griel, P. Le; Ducouret, G.; Brennich, M.; Cristiglio, V.; Roelants, S. L. K. W.; Soetaert, W. Bio-Based Glyco-Bolaamphiphile Forms a Temperature-Responsive Hydrogel with Tunable Elastic Properties. *Soft Matter* **2018**, *14*, 7859–7872.

(13) Draper, E. R.; Adams, D. J. Low-Molecular-Weight Gels: The State of the Art. *Chem* **2017**, *3*, 390–410.

(14) Estroff, L. a; Hamilton, A. D. Water Gelation by Small Organic Molecules. *Chem. Rev.* **2004**, *104*, 1201–1218.

(15) Shigemitsu, H.; Hamachi, I. Design Strategies of Stimuli-Responsive Supramolecular Hydrogels Relying on Structural Analyses and Cell-Mimicking Approaches. *Acc. Chem. Res.* **2017**, *50*, 740–750.

(16) Yoshida, R.; Okano, T. Stimuli-Responsive Hydrogels and Their Application to Functional Materials. In *Biomedical Applications of Hydrogels Handbook*; Ottenbrite, R. M., Park, K., Okano, T., Eds.; Spinger, 2010; Vol. c, pp 19–43.

(17) Raeburn, J.; Zamith Cardoso, A.; Adams, D. J. The Importance of the Self-Assembly Process to Control Mechanical Properties of Low Molecular Weight Hydrogels. *Chem. Soc. Rev.* **2013**, *42*, 5143–5156.

(18) Menger, F. M.; Caran, K. L. Anatomy of a Gel. Amino Acid Derivatives That Rigidify Water at Submillimolar Concentrations. *J. Am. Chem. Soc.* **2000**, *122*, 11679–11691.

(19) Köhler, K.; Meister, A.; Förster, G.; Dobner, B.; Drescher, S.; Ziethe, F.; Richter, W.; Steiniger, F.; Drechsler, M.; Hause, G.; et al. Conformational and Thermal Behavior of a PH-Sensitive Bolaform Hydrogelator. *Soft Matter* **2006**, *2*, 77.

(20) Meister, A.; Bastrop, M.; Koschoreck, S.; Garamus, V. M.; Sinemus, T.; Hempel, G.; Drescher, S.; Dobner, B.; Richtering, W.; Huber, K.; et al. Structure-Property Relationship in Stimulus-Responsive Bolaamphiphile Hydrogels. *Langmuir* **2007**, *23*, 7715–7723.

(21) Li, H.; Yang, P.; Pageni, P.; Tang, C. Recent Advances in Metal-Containing Polymer Hydrogels. *Macromol. Rapid Commun.* **2017**, *38*, 1700109.

(22) Hartgerink, J. D.; Beniash, E.; Stupp, S. I. Peptide-Amphiphile Nanofibers: A Versatile Scaffold for the Preparation of Self-Assembling Materials. *Proc. Nat. Ac. Sci. USA* **2002**, *99*, 5133–5138.

(23) Zhang, S.; Greenfield, M. A.; Mata, A.; Palmer, L. C.; Bitton, R.; Mantei, J. R.; Aparicio, C.; De La Cruz, M. O.; Stupp, S. I. A Self-Assembly Pathway to Aligned Monodomain Gels. *Nat.*

Mater. **2010**, *9*, 594–601.

(24) Xie, Y.; Zhao, J.; Huang, R.; Qi, W.; Wang, Y.; Su, R.; He, Z. Calcium-Ion-Triggered Co-Assembly of Peptide and Polysaccharide into a Hybrid Hydrogel for Drug Delivery. *Nanoscale Res. Lett.* **2016**, *11*, 184.

(25) Kuosmanen, R.; Rissanen, K.; Sievänen, E. Steroidal Supramolecular Metallogels. *Chem. Soc. Rev.* **2020**, *49*, 1977–1998.

(26) Fu, H. L. K.; Yam, V. W. W. Highlight Review Supramolecular Metallogels of Platinum(II) and Gold(III) Complexes. *Chem. Lett.* **2018**, *47*, 605–610.

(27) Tam, A. Y. Y.; Yam, V. W. W. Recent Advances in Metallogels. *Chem. Soc. Rev.* **2013**, *42*, 1540–1567.

(28) Ji, S.; Xu, L.; Fu, X.; Sun, J.; Li, Z. Light- and Metal Ion-Induced Self-Assembly and Reassembly Based on Block Copolymers Containing a Photoresponsive Polypeptide Segment. *Macromolecules* **2019**, *52*, 4686–4693.

(29) Terech, P.; Weiss, R. G. Low Molecular Mass Gelators of Organic Liquids and the Properties of Their Gels. *Chem. Rev.* **1997**, *97*, 3133–3159.

(30) Hirst, A. R.; Escuder, B.; Miravet, J. F.; Smith, D. K. High-Tech Applications of Self-Assembling Supramolecular Nanostructured Gel-Phase Materials: From Regenerative Medicine to Electronic Devices. *Angewandte Chemie - International Edition*. 2008, pp 8002–8018.

(31) Datta, S.; Saha, M. L.; Stang, P. J. Hierarchical Assemblies of Supramolecular Coordination Complexes. *Acc. Chem. Res.* **2018**, *51*, 2047–2063.

(32) Leontidis, E. Chaotropic Salts Interacting with Soft Matter: Beyond the Lyotropic Series. *Curr. Opin. Colloid Interface Sci.* **2016**, *23*, 100–109.

(33) Alargova, R. G.; Danov, K. D.; Kralchevsky, P. A.; Broze, G.; Mehreteab, A. Growth of Giant Rodlike Micelles of Ionic Surfactant in the Presence of Al3+ Counterions. *Langmuir* **1998**, *14*, 4036–4049.

(34) Alargova, R. G.; Ivanova, V. P.; Kralchevsky, P. A.; Mehreteab, A.; Broze, G. Growth of Rod-like Micelles in Anionic Surfactant Solutions in the Presence of Ca2+ Counterions. *Colloids Surfaces A Physicochem. Eng. Asp.* **1998**, *142*, 201–218.

(35) Alargova, R. . G.; Petkov, J. . T.; Petsev, D. . N. Micellization and Interfacial Properties of Alkyloxyethylene Sulfate Surfactants in the Presence of Multivalent Counterions. *J. Colloid Interface Sci.* **2003**, *261*, 1–11.

(36) Chen, L.; Pont, G.; Morris, K.; Lotze, G.; Squires, A.; Serpell, L. C.; Adams, D. J. Salt-Induced Hydrogelation of Functionalised-Dipeptides at High PH. *Chem. Commun.* **2011**, *47*, 12071–12073.

(37) Angelescu, D.; Caldararu, H.; Khan, A. Some Observations on the Effect of the Trivalent Counterion Al3+ to the Self-Assembly of Sodium Dodecyl Sulphate in Water. *Colloids Surfaces A Physicochem. Eng. Asp.* **2004**, *245*, 49–60.

(38) Zhang, F.; Zhang, Q.; Han, C.; Zhang, J.; Yu, M.; Liu, J.; Wei, X. Effect of Aging Time and Salt on the Viscosity Behaviour of a Gemini Cationic Surfactant. *Phys. Chem. Liq.* **2017**, *55*, 492–505.

(39) Vlachy, N.; Drechsler, M.; Verbavatz, J. M.; Touraud, D.; Kunz, W. Role of the Surfactant Headgroup on the Counterion Specificity in the Micelle-to-Vesicle Transition through Salt Addition. *J. Colloid Interface Sci.* **2008**, *319*, 542–548.

(40) Xu, H.; Penfold, J.; Thomas, R. K.; Petkov, J. T.; Tucker, I.; Grillo, I.; Terry, A. Impact of AlCl3 on the Self-Assembly of the Anionic Surfactant Sodium Polyethylene Glycol Monoalkyl Ether Sulfate in Aqueous Solution. *Langmuir* **2013**, *29*, 13359–13366.

(41) Chen, L.; McDonald, T. O.; Adams, D. J. Salt-Induced Hydrogels from Functionalised-Dipeptides. *RSC Adv.* **2013**, *3*, 8714–8720.

(42) Zhou, X. R.; Ge, R.; Luo, S. Z. Self-Assembly of PH and Calcium Dual-Responsive Peptide-Amphiphilic Hydrogel. *J. Pept. Sci.* **2013**, *19*, 737–744.

(43) Greenfield, M. A.; Hoffman, J. R.; De La Cruz, M. O.; Stupp, S. I. Tunable Mechanics of Peptide Nanofiber Gels. *Langmuir* **2010**, *26*, 3641–3647.

(44) Shi, J.; Gao, Y.; Zhang, Y.; Pan, Y.; Xu, B. Calcium Ions to Cross-Link Supramolecular Nanofibers to Tune the Elasticity of Hydrogels over Orders of Magnitude. *Langmuir* **2011**, *27*, 14425–14431.

(45) Kim, J.; Park, C. H.; Kim, S. H.; Yoon, S.; Piao, L. Mechanism of Organogel Formation from Mixed-Ligand Silver (I) Carboxylates. *Bull. Korean Chem. Soc.* **2011**, *32*, 3267–3273.

(46) Bertsch, P.; Isabettini, S.; Fischer, P. Ion-Induced Hydrogel Formation and Nematic Ordering of Nanocrystalline Cellulose Suspensions. *Biomacromolecules* **2017**, *18*, 4060–4066.

(47) Peng, F.; Li, G.; Liu, X.; Wu, S.; Tong, Z. Redox-Responsive Gel-Sol/Sol-Gel Transition in Poly(Acrylic Acid) Aqueous Solution Containing Fe(III) Ions Switched by Light. *J. Am. Chem. Soc.* **2008**, *130*, 16166–16167.

(48) Wu, G. Y.; Liang, C.; Li, H.; Zhang, X.; Yao, G.; Zhu, F. F.; Hu, Y. X.; Yin, G. Q.; Zheng, W.; Lu, Z. A Multi-Responsive Supramolecular Heparin-Based Biohybrid Metallogel Constructed by Controlled Self-Assembly Based on Metal-Ligand, Host-Guest and Electrostatic Interactions. *Org. Chem. Front.* **2021**, *8*, 4715–4722.

(49) Owen, T.; Butler, A. Metallosurfactants of Bioinorganic Interest: Coordination-Induced Self Assembly. *Coord. Chem. Rev.* **2011**, *255*, 678–687.

(50) Baccile, N.; Selmane, M.; Le Griel, P.; Prévost, S.; Perez, J.; Stevens, C. V.; Delbeke, E.; Zibek, S.; Guenther, M.; Soetaert, W.; et al. PH-Driven Self-Assembly of Acidic Microbial Glycolipids. *Langmuir* **2016**, *32*, 6343–6359.

(51) Baccile, N.; Cuvier, A.-S.; Prévost, S.; Stevens, C. V; Delbeke, E.; Berton, J.; Soetaert, W.; Van Bogaert, I. N. A.; Roelants, S. Self-Assembly Mechanism of PH-Responsive Glycolipids: Micelles, Fibers, Vesicles, and Bilayers. *Langmuir* **2016**, *32*, 10881–10894.

(52) Ben Messaoud, G.; Griel, P. Le; Prévost, S.; Merino, D. H.; Soetaert, W.; Roelants, S. L. K. W.; Stevens, C. V.; Baccile, N. Single-Molecule Lamellar Hydrogels from Bolaform Microbial Glucolipids. *Soft Matter* **2020**, *16*, 2528–2539.

(53) Saerens, K. M. J.; Zhang, J.; Saey, L.; Van Bogaert, I. N. A.; Soetaert, W. Cloning and Functional Characterization of the UDP-Glucosyltransferase UgtB1 Involved in Sophorolipid Production by Candida Bombicola and Creation of a Glucolipid-Producing Yeast Strain. *Yeast* **2011**, *28*, 279–292.

(54) Poirier, A.; Griel, P. Le; Hoffmann, I.; Perez, J.; Pernot, P.; Fresnais, J.; Baccile, N. Ca2+ and Ag+ Orient Low-Molecular Weight Amphiphile Self-Assembly into "Nano-Fishnet" Fibrillar Hydrogels with Unusual β-Sheet-like Raft Domains. *Soft Matter* **2022**, DOI: 10.1039/D2SM01218A.

(55) Poirier, A.; Griel, P. Le; Perez, J.; Hermida-Merino, D.; Pernot, P.; Baccile, N. Metallogels from Glycolipid Biosurfactant. *ACS Sustain. Chem. Eng.* **2022**, DOI: 10.1021/acssuschemeng.2c01860.

(56) Poirier, A.; Bizien, T.; Zinn, T.; Pernot, P.; Baccile, N. Shear Recovery and Temperature Stability of Ca2+ and Ag+ Glycolipid Fibrillar Metallogels with Unusual β-Sheet-like Domains. *Soft Matter* **2022**, DOI: 10.1039/d2sm00374k.

(57) Baccile, N.; Pedersen, J. S.; Pehau-Arnaudet, G.; Van Bogaert, I. N. a. Surface Charge of Acidic Sophorolipid Micelles: Effect of Base and Time. *Soft Matter* **2013**, *9*, 4911–4922.

(58) Chen, Q.; Li, Y.; Liu, M.; Zhu, B.; Mu, J.; Chen, Z. Removal of Pb and Hg from Marine Intertidal Sediment by Using Rhamnolipid Biosurfactant Produced by a Pseudomonas Aeruginosa Strain. *Environ. Technol. Innov.* **2021**, *22*, 101456.

(59) Hari, O.; Upadhyay, S. K. Rhamnolipid–Metal Ions (CrVI and PbII) Complexes: Spectrophotometric, Conductometric, and Surface Tension Measurement Studies. *J. Surfactants Deterg.* **2021**, *24*, 281–288.

(60) Mulligan, C. N.; Wang, S. Remediation of a Heavy Metal-Contaminated Soil by a Rhamnolipid Foam. *Eng. Geol.* **2006**, *85*, 75–81.

(61) Miller, R. M. Biosurfactant-Facilitated Remediation of Metal-Contaminated Soils. *Environ. Health Perspect.* **1995**, *103*, 59–62.

(62) Herman, D. C.; Artiola, J. F.; Miller, R. M. Removal of Cadmium, Lead, and Zinc from Soil by a Rhamnolipid Biosurfactant. *Environ. Sci. Technol.* **1995**, *29*, 2280–2285.

(63) Chen, M.; Dong, C.; Penfold, J.; Thomas, R. K.; Smyth, T. J. P.; Perfumo, A.; Marchant, R.; Banat, I. M.; Stevenson, P.; Parry, A.; et al. Influence of Calcium Ions on Rhamnolipid and Rhamnolipid/Anionic Surfactant Adsorption and Self-Assembly. *Langmuir* **2013**, *29*, 3912–3923.

(64) Shen, H.-H. H.; Lin, T.-W. W.; Thomas, R. K.; Taylor, D. J. F. F.; Penfold, J. Surfactin Structures at Interfaces and in Solution: The Effect of PH and Cations. *J. Phys. Chem. B* **2011**, *115*, 4427–

4435.

(65) Dahrazma, B.; Mulligan, C. N.; Nieh, M. P. Effects of Additives on the Structure of Rhamnolipid (Biosurfactant): A Small-Angle Neutron Scattering (SANS) Study. *J. Colloid Interface Sci.* **2008**, *319*, 590–593.

(66) Baccile, N.; Poirier, A.; Seyrig, C.; Griel, P. Le; Perez, J.; Hermida-Merino, D.; Pernot, P.; Roelants, S.; Soetaert, W. Chameleonic Amphiphile: The Unique Multiple Self-Assembly Properties of a Natural Glycolipid in Excess of Water. *J. Colloid Interface Sci.* **2023**, *630*, 404–415.

(67) Gradzielski, M.; Grillo, I.; Narayanan, T. Dynamics of Structural Transitions in Amphiphilic Systems Monitored by Scattering Techniques. *Prog. Colloid Polym. Sci.* **2004**, *129*, 32–39.

(68) Gradzielski, M. Investigations of the Dynamics of Morphological Transitions in Amphiphilic Systems. *Curr. Opin. Colloid Interface Sci.* **2004**, *9*, 256–263.

(69) Rosén, T.; Wang, R.; He, H.; Zhan, C.; Chodankar, S.; Hsiao, B. S. Understanding Ion-Induced Assembly of Cellulose Nanofibrillar Gels through Shear-Free Mixing and: In Situ Scanning-SAXS. *Nanoscale Adv.* **2021**, *3*, 4940–4951.

(70) Panine, P.; Finet, S.; Weiss, T. M.; Narayanan, T. Probing Fast Kinetics in Complex Fluids by Combined Rapid Mixing and Small-Angle X-Ray Scattering. *Adv. Colloid Interface Sci.* **2006**, *127*, 9–18.

(71) Moitzi, C.; Guillot, S.; Fritz, G.; Salentinig, S.; Glatter, O. Phase Reorganization in Self-Assembled Systems through Interparti Cle Material Transfer. *Adv. Mater.* **2007**, *19*, 1352–1358.

(72) Michaux, F.; Baccile, N.; Impéror-Clerc, M.; Malfatti, L.; Folliet, N.; Gervais, C.; Manet, S.; Meneau, F.; Pedersen, J. S.; Babonneau, F. In Situ Time-Resolved SAXS Study of the Formation of Mesostructured Organically Modified Silica through Modeling of Micelles Evolution during Surfactant-Templated Self-Assembly. *Langmuir* **2012**, *28*, 17477–17493.

(73) Yaghmur, A.; Laggner, P.; Sartori, B.; Rappolt, M. Calcium Triggered Lα-H2 Phase Transition Monitored by Combined Rapid Mixing and Time-Resolved Synchrotron SAXS. *PLoS One* **2008**, *3*.

(74) Dhasaiyan, P.; Prévost, S.; Baccile, N.; Prasad, B. L. V. PH- and Time-Resolved in-Situ SAXS Study of Self-Assembled Twisted Ribbons Formed by Elaidic Acid Sophorolipids. *Langmuir* **2018**, *34*, 2121–2131.

(75) Schindelin, J.; Arganda-Carreras, I.; Frise, E.; Kaynig, V.; Longair, M.; Pietzsch, T.; Preibisch, S.; Rueden, C.; Saalfeld, S.; Schmid, B.; et al. Fiji: An Open-Source Platform for Biological-Image Analysis. *Nat. Methods* **2012**, *9*, 676–682.

(76) Cui, H.; Muraoka, T.; Cheetham, A. G.; Stupp, S. I. Self-Assembly of Giant Peptide Nanobelts. *Nano Lett.* **2009**, *9*, 945–951.

(77) Stradner, A.; Glatter, O.; Schurtenberger, P. Hexanol-Induced Sphere-to-Flexible Cylinder Transition in Aqueous Alkyl Polyglucoside Solutions. *Langmuir* **2000**, *16*, 5354–5364.

(78) Zhang, R.; Marone, P. A.; Thiyagarajan, P.; Tiede, D. M. Structure and Molecular Fluctuations of N-Alkyl-β-D-Glucopyranoside Micelles Determined by X-Ray and Neutron Scattering. *Langmuir* **1999**, *15*, 7510–7519.

(79) Wei, Y.; Hore, M. J. A. Characterizing Polymer Structure with Small-Angle Neutron Scattering: A Tutorial. *J. Appl. Phys.* **2021**, *129*.

(80) Jensen, G. V.; Lund, R.; Gummel, J.; Narayanan, T.; Pedersen, J. S. Monitoring the Transition from Spherical to Polymer-like Surfactant Micelles Using Small-Angle X-Ray Scattering. *Angew. Chemie Int. Ed.* **2014**, *53*, 11524–11528.

(81) Baccile, N.; Babonneau, F.; Jestin, J.; Pehau-Arnaudet, G.; Van Bogaert, I.; Péhau-Arnaudet, G.; Van Bogaert, I.; Pehau-Arnaudet, G.; Van Bogaert, I. Unusual, PH-Induced, Self-Assembly of Sophorolipid Biosurfactants. *ACS Nano* **2012**, *6*, 4763–4776.

(82) Friedrich, H.; Frederik, P. M.; De With, G.; Sommerdijk, N. A. J. M. Imaging of Self-Assembled Structures: Interpretation of TEM and Cryo-TEM Images. *Angew. Chemie - Int. Ed.* **2010**, *49*, 7850–7858.

(83) Maire du Poset, A.; Zitolo, A.; Cousin, F.; Assifaoui, A.; Lerbret, A. Evidence for an Egg-Box-like Structure in Iron(II)-Polygalacturonate Hydrogels: A Combined EXAFS and Molecular Dynamics Simulation Study. *Phys. Chem. Chem. Phys.* **2020**, *22*, 2963–2977.

(84) Grant, G. T.; Morris, E. R.; Rees, D. A. BIOLOGICAL INTERACTIONS BETWEEN POLYSACCHARtDES AND DIVALENT CATIONS: THE EGG-BOX MODEL. *FEBS Lett.* **1973**, *32*, 195–198.

(85) Fang, Y.; Al-Assaf, S.; Phillips, G. O.; Nishinari, K.; Funami, T.; Williams, P. A.; Li, A. Multiple Steps and Critical Behaviors of the Binding of Calcium to Alginate. *J. Phys. Chem. B* **2007**, *111*, 2456–2462.

(86) Srinivasan, V.; Blankschtein, D. Effect of Counterion Binding on Micellar Solution Behavior: 2. Prediction of Micellar Solution Properties of Ionic Surfactant-Electrolyte Systems. *Langmuir* **2003**, *19*, 9946–9961.

(87) Qiao, Y.; Lin, Y.; Wang, Y.; Li, Z.; Huang, J. Metal-Driven Viscoelastic Wormlike Micelle in Anionic/Zwitterionic Surfactant Systems and Template-Directed Synthesis of Dendritic Silver Nanostructures. *Langmuir* **2011**, *27*, 1718–1723.

(88) Si, Y.; Wang, L.; Wang, X.; Tang, N.; Yu, J.; Ding, B. Ultrahigh-Water-Content, Superelastic, and Shape-Memory Nanofiber-Assembled Hydrogels Exhibiting Pressure-Responsive Conductivity. *Adv. Mater.* **2017**, *29*, 1–7.

(89) Davidson, G. J. E.; Tong, L. H.; Raithby, P. R.; Sanders, J. K. M. Aluminium(III) Porphyrins as Supramolecular Building Blocks. *Chem. Commun.* **2006**, No. 29, 3087–3089.

(90) Baes, C. F.; Mesmer, R. E. *The Hydrolysis of Cations*; John Wiley & Sons, Inc.: New York, London, Sydney, Toronto, 1976.

(91) Lincoln, S. F.; Richens, D. T.; Sykes, A. G. Metal Aqua Ions. In *Comprehensive Coordination*

Chemistry II; 2003; pp 515–555.

(92) Jian-Xiao, L. V.; Dong, W.; Ji-Ti, Z. Interaction Mechanisms between Anionic Surfactant Micelles and Different Metal Ions in Aqueous Solutions. *J. Dispers. Sci. Technol.* **2006**, *27*, 1073–1077.

(93) Glatter, O.; Kratky, O. *Small Angle X-Ray Scattering*; Academic Press: London, 1982.

(94) Teixeira, J. Small-Angle Scattering by Fractal Systems. *J. Appl. Crystallogr.* **1988**, *21*, 781–785.

(95) Zou, A.; Liu, J.; Garamus, V. M.; Yang, Y.; Willumeit, R.; Mu, B. Micellization Activity of the Natural Lipopeptide [Glui, Asp5] Surfactin-C15 in Aqueous Solution. *J. Phys. Chem. B* **2010**, *114*, 2712–2718.

(96) Vasilescu, M.; Angelescu, D.; Caldararu, H.; Almgren, M.; Khan, A. Fluorescence Study on the Size and Shape of Sodium Dodecyl Sulphate-Aluminium Salt Micelles. *Colloids Surfaces A Physicochem. Eng. Asp.* **2004**, *235*, 57–64.

(97) Penfold, J.; Thomas, R. K.; Dong, C. C.; Tucker, I.; Metcalfe, K.; Golding, S.; Grillo, I. Equilibrium Surface Adsorption Behavior in Complex Anionic/Nonionic Surfactant Mixtures. *Langmuir* **2007**, *23*, 10140–10149.

(98) Bi, S.; Wang, C.; Cao, Q.; Zhang, C. Studies on the Mechanism of Hydrolysis and Polymerization of Aluminum Salts in Aqueous Solution: Correlations between the "Core-Links" Model and "Cage-like" Keggin-Al13 Model. *Coord. Chem. Rev.* **2004**, *248*, 441–455.

(99) Bottero, J. Y.; Tchoubar, D.; Cases, J. M.; Fiessinger, F. Investigation of the Hydrolysis of Aqueous Solutions of Aluminum Chloride. 2. Nature and Structure by Small-Angle X-Ray Scattering. *J. Phys. Chem.* **1982**, *86*, 3667–3673.

(100) Fulton, B. L. Synthesis of Aqueous Inorganic Nanoscale Clusters and How Their Coordination Geometries Affect Solution Speciation and Thin Film Properties, University of Oregon, 2019.

(101) Moyer, T. J.; Cui, H.; Stupp, S. I. Tuning Nanostructure Dimensions with Supramolecular Twisting. *J. Phys. Chem. B* **2013**, *117*, 4604–4610.

(102) Yu, D.; Wang, Y.; Zhang, J.; Tian, M.; Han, Y.; Wang, Y. Effects of Calcium Ions on Solubility and Aggregation Behavior of an Anionic Sulfonate Gemini Surfactant in Aqueous Solutions. *J. Colloid Interface Sci.* **2012**, *381*, 83–88.

(103) Diener, M.; Adamcik, J.; Bergfreund, J.; Catalini, S.; Fischer, P.; Mezzenga, R. Rigid, Fibrillar Quaternary Structures Induced by Divalent Ions in a Carboxylated Linear Polysaccharide. *ACS Macro Lett.* **2020**, *9*, 115–121.

(104) Israelachvili, J. N.; Mitchell, D. J. A Model for the Packing of Lipids in Bilayer Membranes. *Biochim. Biophys. Acta* **1975**, *389*, 13–19.

(105) Israelachvili, J. N.; Ninham, B. W.; Mitchell, D. J. Theory of Self-Assembly of Lipids and Vesicles. *Biochim. Biophys. Acta* **1977**, *470*, 185–201.

(106) Loh, W.; Brinatti, C.; Tam, K. C. Use of Isothermal Titration Calorimetry to Study Surfactant Aggregation in Colloidal Systems. *Biochim. Biophys. Acta - Gen. Subj.* **2016**, *1860*, 999–1016.

(107) Sinn, C. G.; Dimova, R.; Antonietti, M. Isothermal Titration Calorimetry of the Polyelectrolyte/Water Interaction and Binding of Ca2+: Effects Determining the Quality of Polymeric Scale Inhibitors. *Macromolecules* **2004**, *37*, 3444–3450.

(108) Chiad, K.; Stelzig, S. H.; Gropeanu, R.; Weil, T.; Klapper, M.; Muüllen, K. Isothermal Titration Calorimetry: A Powerful Technique to Quantify Interactions in Polymer Hybrid Systems. *Macromolecules* **2009**, *42*, 7545–7552.

(109) Seyrig, C.; Kignelman, G.; Thielemans, W.; Griel, P. Le; Cowieson, N.; Perez, J.; Baccile, N. Stimuli-Induced Non-Equilibrium Phase Transitions in Polyelectrolyte-Surfactant Complex Coacervates. *Langmuir* **2020**, *36*, 8839–8857.

(110) Lehrmann, R.; Seelig, J. Adsorption of Ca2+ and La3+ to Bilayer Membranes: Measurement of the Adsorption Enthalpy and Binding Constant with Titration Calorimetry. *BBA - Biomembr.* **1994**, *1189*, 89–95.

(111) Du, C.; Cai, D.; Qin, M.; Zheng, P.; Hao, Z.; Yin, T.; Zhao, J.; Shen, W. Thermodynamics of Mixed Surfactant Solutions of N, N ′- Bis(Dimethyldodecyl)-1,2-Ethanediammoniumdibromide with 1-Dodecyl-3- Methylimidazolium Bromide. *J. Phys. Chem. B* **2014**, *118*, 1168–1179.

(112) Ito, T. H.; Rodrigues, R. K.; Loh, W.; Sabadini, E. Calorimetric and Light Scattering Investigations of the Transition from Spherical to Wormlike Micelles of C14TAB Triggered by Salicylate. *Langmuir* **2015**, *31*, 6020–6026.

(113) Johnson, R. A.; Manley, O. M.; Spuches, A. M.; Grossoehme, N. E. Dissecting ITC Data of Metal Ions Binding to Ligands and Proteins. *Biochim. Biophys. Acta* **2016**, *1860*, 892–901.

(114) Assifaoui, A.; Lerbret, A.; Uyen, H. T. D.; Neiers, F.; Chambin, O.; Loupiac, C.; Cousin, F. Structural Behaviour Differences in Low Methoxy Pectin Solutions in the Presence of Divalent Cations (Ca2+and Zn2+): A Process Driven by the Binding Mechanism of the Cation with the Galacturonate Unit. *Soft Matter* **2015**, *11*, 551–560.

(115) Löf, D.; Niemiec, A.; Schillén, K.; Loh, W.; Olofsson, G. A Calorimetry and Light Scattering Study of the Formation and Shape Transition of Mixed Micelles of EO20PO68EO20 Triblock Copolymer (P123) and Nonionic Surfactant (C12EO6). *J. Phys. Chem. B* **2007**, *111*, 5911–5920.

(116) Katz, A. K.; Glusker, J. P.; Beebe, S. A.; Bock, C. W. Calcium Ion Coordination: A Comparison with That of Beryllium, Magnesium, and Zinc. *J. Am. Chem. Soc.* **1996**, *118*, 5752–5763.

(117) Cuvier, A. S.; Babonneau, F.; Berton, J.; Stevens, C. V.; Fadda, G. C.; Genois, I.; Le Griel, P.; Péhau-Arnaudet, G.; Baccile, N. Synthesis of Uniform, Monodisperse, Sophorolipid Twisted Ribbons. *Chem. - An Asian J.* **2015**, *10*, 2419–2426.

(118) Barclay, T. G.; Constantopoulos, K.; Matisons, J. Nanotubes Self-Assembled from Amphiphilic Molecules via Helical Intermediates. *Chem. Rev.* **2014**, *114*, 10217–10291.

(119) Ringbom, A. *Complexation in Analytical Chemistry*; John Wiley & Sons, Inc.: New York, 1963.

(120) Tolochko, B. P.; Chernov, S. V.; Nikitenko, S. G.; Whitcomb, D. R. EXAFS Determination of the Structure of Silver Stearate, [Ag(O2C(CH2)16CH3]2, and the Effect of Temperature on the

Silver Coordination Sphere. *Nucl. Instruments Methods Phys. Res. Sect. A Accel. Spectrometers, Detect. Assoc. Equip.* **1998**, *405*, 428–434.

(121) Maire Du Poset, A.; Lerbret, A.; Boué, F.; Zitolo, A.; Assifaoui, A.; Cousin, F. Tuning the Structure of Galacturonate Hydrogels: External Gelation by Ca, Zn, or Fe Cationic Cross-Linkers. *Biomacromolecules* **2019**, *20*, 2864–2872.

(122) Guo, J.; Li, Y.; Zhang, Y.; Ren, J.; Yu, X.; Cao, X. Switchable Supramolecular Configurations of Al3+/LysTPY Coordination Polymers in a Hydrogel Network Controlled by Ultrasound and Heat. *ACS Appl. Mater. Interfaces* **2021**, *13*, 40079–40087.

(123) Huynh, U. T. D.; Lerbret, A.; Neiers, F.; Chambin, O.; Assifaoui, A. Binding of Divalent Cations to Polygalacturonate: A Mechanism Driven by the Hydration Water. *J. Phys. Chem. B* **2016**, *120*, 1021–1032.

TOC Graphics